Phase I Report

Cover Page

Stable Perovskite Core-Shell Nanocrystals as Down-Converting Phosphors for Solid State Lighting

DOE Funding Opportunity Number: DE-FOA-0001770

CFDA Number: 81.049

Award number: DE-SC0018611

Program Area of Interest: Office of Basic Energy Sciences
14. Performance and Manufacturing Advancements for LEDs and OLEDs for Solid-state Lighting a. LEDs

Reported by:

Team Member Organizations:

PhosphorTech Corporation (Small Business)

Georgia Institute of Technology (University)

Principal Investigator & Technical Point of Contact
Dr. Hisham Menkara, CEO
Email: hisham@phosphortech.com Phone: (404) 664-5008

Business Point of Contact
Dr. Christopher J. Summers, President Emeritus
Email: chris@phosphortech.com Phone: (770) 312-0998

Technical Point of Contact at Georgia Tech
Dr. Zhitao Kang; Email: zhitao.kang@gtri.gatech.edu Phone: (404) 407-6109
Dr. Zhiqun Lin; Email: zhiqun.lin@mse.gatech.edu Phone: (404) 385-4404

Abstract:

Two effective and unique strategies to improve the stabilities of perovskite NCs for solid state lighting (SSL) applications were developed and successfully demonstrated in Phase I grant. ***Perovskite NCs with quantum yield (QY) up to 81% and green emission bandwidth as narrow as 17.7 nm, and RadiantFlex sheets with luminous efficacy of radiation (LER) up to 332 lm/W*** were prepared. They demonstrated proof of principle feasibility leading to the fabrication of white light emitting diodes (WLEDs) with high CRI and wide color gamut.

Background:

Perovskites represent an emerging class of materials by a generic chemical formula ABX_3 with A^+ = methylammonium ($CH_3NH_3^+$), formamidinium ($HC(NH_2)_2^+$), Cs, or their combination; B^{2+} = Pb^{2+} and/or Sn^{2+}; X^- = Cl,$^-$ Br^- and/or I^-. Perovskite thin films have been the focus of perovskite research over the past decade for a variety of optoelectronic applications due largely to their long carrier lifetime, low defect density, composition-dependent tunable bandgaps, narrow full width at half maximum (FWHM), outstanding quantum yield, and low production cost.[1-4] For example, much effort has been centered on increasing the grain size in the perovskite photoactive layer for achieving high-performance perovskite solar cells (PSCs).[5-10] Recently, perovskite nanocrystals (NCs)[11] have garnered tremendous attention owing to their broad visible-to-near infrared wavelength tunability (400-800 nm) and narrow band emission[12-14] for use in lasers,[15-17] electroluminescence devices,[12,16] sensors,[18] and solar cells.[14] Among perovskite NCs, all inorganic $CsPbX_3$ NCs possess narrow FWHM of emission (as small as 12 nm) and excellent quantum yield (50%~90%).[11,19,20] They have a Bohr diameter up to 12 nm,[11] exhibiting a size-tunable bandgap in the visible region. It is also notable that the exchange of halide ions (Cl^-, Br^- and I^-) in as-synthesized perovskite NCs is highly effective, rendering easy and rapid access to a wide range of perovskite NCs with tunable absorption and photoluminescence (PL) spectra.[11,21]

Despite significant progress that has been achieved in the synthesis of $CsPbX_3$ NCs, it remains a grand challenge to achieve their practical application for solid state lighting (SSL) as they suffer from intrinsic chemical instability.[22] First, their ionic character suggests poor moisture tolerance.[23,24] $CsPbX_3$ NCs degrade rapidly in the presence of moisture. Second, the weakly-bounded surface ligands, typically in the form of an ion pair of carboxylic acid and amine,[25] are easily dissociated from the surface of NCs during purification with anti-solvents, thereby resulting in greatly reduced colloidal stability and PLQY of NCs.[26,27] Third, a fast yet unavoidable anion exchange occurs when mixing $CsPbX_3$ NCs of different compositions, leading to composition homogenization.[28] For example, mixing of $CsPbBr_3$ and $CsPbI_3$ NCs yields $CsPbBr_xI_{3-x}$ NCs, and their emission is situated between the respective emissions of the two constituents.[29,30,31] Fourth, phase instability of $CsPbX_3$ NCs is also a widely recognized issue. Notably, it has been reported that all $CsPbX_3$ NCs crystallize in their cubic phase and remain stable in this phase owing to high synthesis temperature and the contributions from surface energy.[32] For $CsPbI_3$ NCs, however, their perovskite phase (e.g., cubic phase) was found to be metastable under ambient condition. As a result, they undergo a rapid cubic-to-orthorhombic phase transition, thus diminishing their fluorescent properties.[33,34] This is not surprising because orthorhombic phase is thermodynamically stable for bulk $CsPbI_3$ material below 315 °C.[32] Finally, for all-inorganic mixed-halide perovskites, for example, $CsPbBr_xI_{3-x}$ NCs, they are ubiquitously plagued by phase segregation, leading to the degradation of emission.[35]

Clearly, there is a tremendous need to improve the stability of $CsPbX_3$ NCs for rendering their commercially viable applications for SSL. To this end, many efforts have recently been centered on addressing the instability issues noted above, including coating $CsPbX_3$ NCs with polyhedral oligomeric silsesquioxane,[36] incorporating $CsPbX_3$ NCs in mesoporous silica,[37] purifying $CsPbI_3$ NCs using methyl acetate as anti-solvent to prevent the dissociation of surface ligands during the purification process,[38] coating with alumina by atomic layer deposition[39] or partial coating with SiO_2 via the sol-gel process,[40] physical mixing with hydrophobic polymers,[6,31,41,42] and encapsulation within polymer beads[24] have proven to be effective in improving stability in polar and ambient environments. However, an effective coating method suitable for large-scale fabrication and homogenous distribution of NCs in the matrix, as well as methods for hermetic protection of NCs at single particle level, are not available.

Herein, we report on two effective and unique strategies to improve the instabilities of perovskite nanocrystals. The first approach was aimed at producing $CsPbX_3$ NCs with greatly improved water, compositional, phase, and phase segregation stabilities by impregnating them within solid organic salt matrices (i.e., metal stearate (MSt)), that is, forming $CsPbX_3$–MSt nanocomposites. MSt used in our study includes aluminum stearate ($AlSt_3$), zinc stearate ($ZnSt_2$), and sodium stearate (NaSt). The introduction of MSt solid into $CsPbX_3$ NCs solution leads to the co-precipitation of MSt (NaSt, $ZnSt_2$, and $AlSt_3$) and $CsPbX_3$ NCs. The subsequent centrifugation process readily removes the excessive ligands and precursors without the need of using anti-solvents. The resulting $CsPbX_3$–MSt nanocomposites exhibit excellent optical properties with an impressive set of high stabilities. First, water stability is manifested in the retention of high photoluminescence of $CsPbX_3$–MSt nanocomposites (except NaSt as it is water-soluble) in the presence of water due to the insolubility of MSt in water and the impregnation of $CsPbX_3$ by MSt. Second, compositional stability is demonstrated by the retention of two distinct emission peaks from $CsPbBr_3$ and $CsPbI_3$ NCs, respectively, when mixing separately prepared $CsPbBr_3$–MSt and $CsPbI_3$–MSt nanocomposites together. In other words, no anion exchange between $CsPbBr_3$ and $CsPbI_3$ NCs occurs as MSt effectively encapsulates and isolates $CsPbBr_3$ and $CsPbI_3$ NCs. Third, phase stability is revealed by the preservation of emission of $CsPbI_3$ NCs in MSt due to the released lattice strain by the wraparound MSt matrices, preventing it from phase transformation from the emissive cubic phase to non-emissive orthorhombic phase. Consequently, $CsPbI_3$ NCs in $CsPbI_3$–MSt nanocomposites maintain their cubic phase and high emission for at least one month. Finally, phase segregation stability is signified by the appearance of pure and stable photoluminescence of $CsPbBr_{1.5}I_{1.5}$ NCs as the possible phase segregation of $CsPbBr_3$ and $CsPbI_3$ NCs is suppressed probably by the released lattice strain as well as owing to the MSt encapsulation. A representative WLED composed of $CsPbX_3$–MSt nanocomposites excited by a blue InGaN LED chip was constructed, displaying high color rendering index (Ra) and a low color temperature (Tc). Taken together, the results of this study exemplify that metal stearates are an attractive class of matrix materials for stabilizing perovskite $CsPbX_3$ NCs via co-precipitation of $CsPbX_3$ NCs and MSt, yielding highly stable fluorescent solid-state materials and can be used as powder phosphors for SSL applications.

The second approach was aimed at developing a general and robust strategy by capitalizing on judiciously designed amphiphilic star-like diblock copolymers with well-controlled molecular weight and low polydispersity of each block as molecularly engineered nanoreactors to craft uniform perovskite NCs. Remarkably, these NCs simultaneously possess precisely tunable

dimensions and considerably enhanced colloidal and water stabilities for SSL applications via an extremely facile and rapid co-precipitation reaction. The amphiphilic star-like diblock copolymer nanoreactors exploited are poly(acrylic acid)-*block*-polystyrene (denoted PAA-*b*-PS) synthesized by atom transfer radical polymerization (ATRP), comprising hydrophilic inner PAA and hydrophobic outer PS block of different lengths. The selective partition of precursors within the compartment occupied by PAA blocks of star-like diblock copolymers due to strong coordination interaction between the carboxylic acid groups of PAA blocks in star-like PAA-*b*-PS nanoreactors and perovskite precursors (i.e., CsX and PbX_2) yields *in-situ* hairy all-inorganic perovskite $CsPbX_3$ NCs perpetually ligated by hydrophobic PS blocks via the co-precipitation of two precursors in the nonpolar solvent. It is noteworthy that as the molecular weight of PAA and PS blocks can be readily tuned by varying their respective ATRP reaction times. This, in turn, presents the twofold advantages, that is, simple yet reliable control over the diameter of $CsPbX_3$ NCs governed by the length of the inner PAA blocks, thereby leading to precisely size-tunable optical properties, and concurrently outstanding water and colloidal stabilities of $CsPbX_3$ NCs dictated by the length of the outer PS blocks. It is important to note that the outer PS blocks are originally covalently connected to the inner PAA blocks, so the surface capping of $CsPbX_3$ NCs with PS blocks is intimate and permanent (i.e., PS-capped $CsPbX_3$), ensuring excellent colloidal stability in nonpolar solvents and preventing NCs from aggregation. This contrasts sharply to conventional ligand-assisted methods, where ligands are non-covalently bonded to NCs, thus promoting agglomeration of NCs due to the dynamic association-dissociation of surface ligands over time. Moreover, the permanently attached outer PS block forms a protective hydrophobic shell around perovskite NC where the thickness of shell depends on the length of the PS blocks, thereby assuring greatly enhanced stability against polar solvents (e.g., water). These PS-capped $CsPbX_3$ NCs are then utilized for white light emitting diode (WLED), displaying a 116% and a 163% color gamut over that of national television system committee (NTSC) and standard red green blue (sRGB) standards, respectively. In addition to WLED for display backlight and solid state lighting, this intriguing class of stable "hairy" perovskite NCs may find great potential for use in perovskite solar cells, scintillators, bioimaging, biosensors, etc.

1. Stability enhancement of perovskite NCs via encapsulation in hydrophobic metal stearate

A set of $CsPbX_3$ NCs (X = Br, Br/I, and I) were synthesized (see *Experimental Section*). **Figure 1a** shows the UV-Vis and PL spectra of $CsPbBr_3$ NCs in toluene synthesized at 160 °C, with a band edge at 498 nm and exhibiting a PL emission peak at 517 nm (i.e., green emission). These green-emitting NCs have a finite FWHM of 30 nm, indicating a narrow size distribution. The PLQY of $CsPbBr_3$ NCs is 81 %. Their crystal structure is shown in **Figure 1b**. The standard XRD pattern of bulk $CsPbBr_3$ is also included as a reference. The emergence of crystal planes of (100), (110), (200), (211) and (220) suggest the formation of a cubic phase of $CsPbBr_3$ NCs. As-synthesized $CsPbBr_3$ NCs possess the cubic shape with an average size of 10.5 nm (**Figure 1c**). HRTEM of $CsPbBr_3$ NCs is shown in **Figure 1d**. The interplanar distance is measured to be 0.59 nm, which coincides with the (100) plane of $CsPbBr_3$ NCs. For $CsPbBr_{1.5}I_{1.5}$ NCs synthesized at 160 °C, their toluene solution is orange-emitting under UV irradiation, and their PL emission peak is centered at 612 nm with the FWHM of 32 nm and a PLQY of 67 %. The average size of cubic-shaped $CsPbBr_{1.5}I_{1.5}$ NCs is approximately 11.0 nm. The XRD measurement shows that

$CsPbBr_{1.5}I_{1.5}$ NCs have the cubic phase. Similarly, $CsPbI_3$ NCs synthesized at 120 °C have a PL emission peak at 664 nm with a FWHM of 39 nm and PLQY of 52 %, thus emitting a red fluorescence upon UV excitation. They are also cubic-shaped as well with an average size of 9.6 nm and have cubic phase.

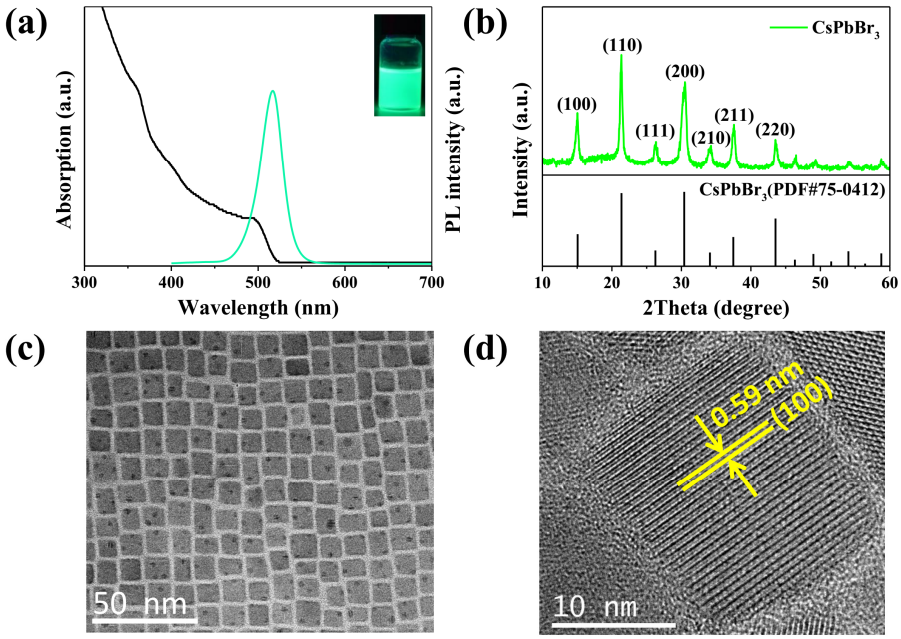

Figure 1. (a) UV-Vis absorption and photoluminescence spectra of $CsPbBr_3$ NCs. Inset: digital image of $CsPbBr_3$ NCs dispersed in toluene under irradiation of 365 nm UV light. (b) XRD pattern of $CsPbBr_3$ NCs (green curve). The standard XRD pattern of bulk $CsPbBr_3$ material is also included for comparison (black curve). (c) TEM image of $CsPbBr_3$ NCs with an average size of 10.5 nm, scale bar=50 nm. (d) HRTEM image of $CsPbBr_3$ NCs, scale bar=10 nm.

Figure 2a depicts the stepwise formation of $CsPbX_3$–MSt nanocomposites. The MSt powder is added into a OLA-capped $CsPbX_3$ NCs toluene solution. The organic salts (MSt) rapidly precipitate together with $CsPbX_3$ NCs from the mixed dispersion solution within several minutes (i.e., co-precipitation of $CsPbBr_3$ NCs and MSt). We speculate that MSt may bind the surface of $CsPbX_3$ NCs via not only the coordination bonding of St–Cs and St–Pb (i.e., replacing the original OLA ligands), but also the ionic interaction between metal ions in MSt and X^- in $CsPbX_3$, as will be further discussed later, thus leading to the co-precipitation of MSt and $CsPbBr_3$ NCs. Such behavior is evidenced by the weak PL from the supernatant while the precipitates (i.e., $CsPbX_3$–MSt nanocomposites) emits bright fluorescence under 365 nm UV light excitation. After collecting the precipitates by centrifugation, they were dried in an oven to yield the final product which can be used as powder phosphors.

Digital images of as-prepared $CsPbBr_3$, $CsPbBr_{1.5}I_{1.5}$ and $CsPbI_3$ NCs toluene solutions and the corresponding $CsPbI_3$–$AlSt_3$, $CsPbBr_{1.5}I_{1.5}$–$AlSt_3$, and $CsPbI_3$–$AlSt_3$ nanocomposites are shown in **Figure 2b**. Cyan-emitting $CsPbBr_3$–$AlSt_3$, orange-emitting $CsPbBr_{1.5}I_{1.5}$–$AlSt_3$ and red-emitting $CsPbI_3$–$AlSt_3$ nanocomposites demonstrate similar color compared to as-prepared perovskite NCs toluene solutions under UV light excitation. **Figure 2c** shows the PL spectra of $CsPbX_3$ NCs in toluene and the corresponding $CsPbX_3$–MSt nanocomposites in the dry state as

powder phosphors, respectively. The PL peaks are centered at 521 nm for $CsPbBr_3$–$AlSt_3$, 621 nm for $CsPbBr_{1.5}I_{1.5}$–$AlSt_3$, and 670 nm for $CsPbI_3$–$AlSt_3$, respectively, in their dry states, representing a slight red-shift compared to their NC toluene solution counterparts. This is likely due to a closer proximity between perovskite NCs when impregnated in $AlSt_3$.

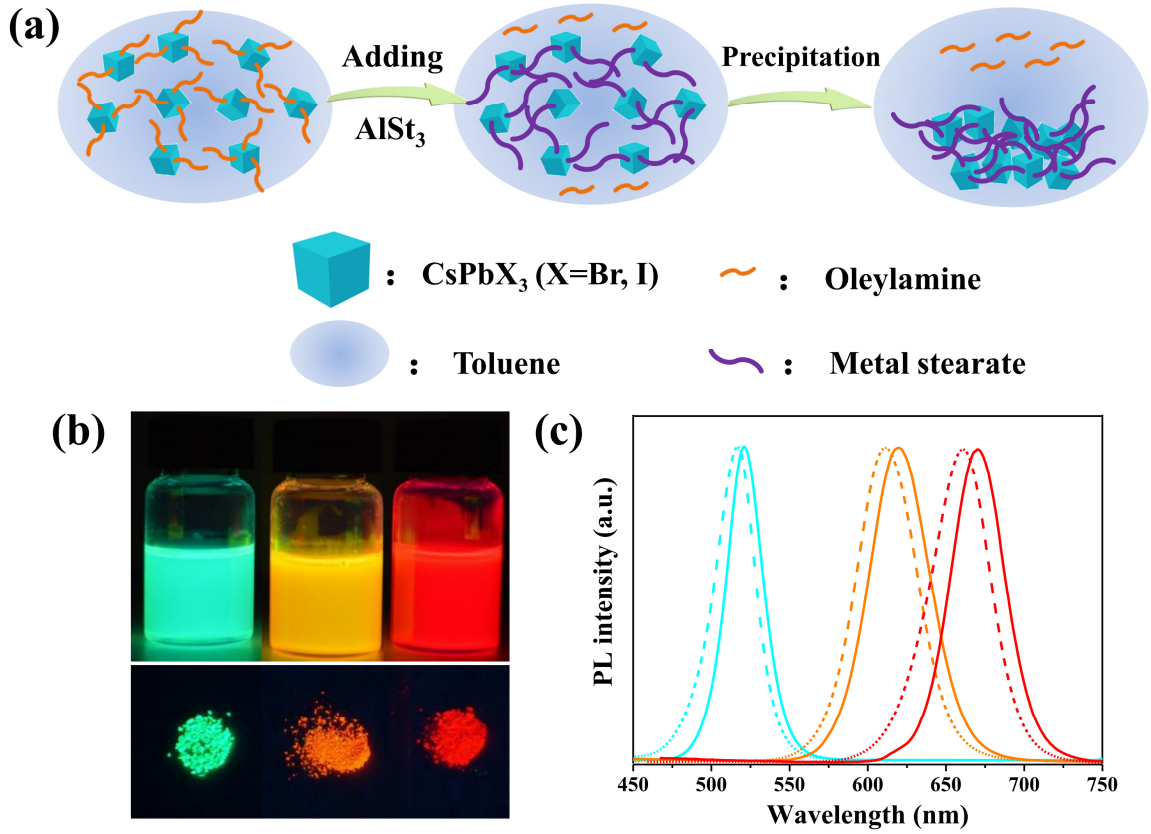

Figure 2. (a) Schematic illustration of the preparation of $CsPbX_3$–MSt nanocomposites by impregnating $CsPbX_3$ in a $AlSt_3$ matrix via a co-precipitation strategy. (b) Digital images of $CsPbBr_3$ NCs (cyan, upper-left), $CsPbBr_{1.5}I_{1.5}$ NCs (orange, upper-central), $CsPbI_3$ NCs (red, upper-right) dispersed in toluene and the corresponding $CsPbBr_3$ NCs–$AlSt_3$ (cyan, lower-left), $CsPbBr_{1.5}I_{1.5}$–$AlSt_3$ (orange, lower-central), $CsPbI_3$–$AlSt_3$ nanocomposites (red, lower-right) under 365 nm UV light irradiation. (c) PL spectra of $CsPbBr_3$ NCs (cyan, dashed curve), $CsPbBr_{1.5}I_{1.5}$ NCs (orange, dashed curve), $CsPbI_3$ NCs (red, dashed curve) dispersed in toluene. The PL spectra of the corresponding $CsPbX_3$–$AlSt_3$ nanocomposites in the dry states as powder phosphors are shown by solid curves.

It is notable that in addition to $AlSt_3$, other stearate salts (NaSt and $ZnSt_2$) were also investigated. When NaSt was employed to encapsulate $CsPbX_3$ NCs, a red-shift of the PL maximum over the pristine $CsPbX_3$ NCs can be found in the resulting $CsPbX_3$–NaSt nanocomposites. Similarly, such a red-shift is likely due to the increase concentration of $CsPbX_3$ NCs in the nanocomposites compared to the NC solution sample. Interestingly, for $ZnSt_2$ a PL blue-shift was observed in the resulting $CsPbX_3$–$ZnSt_2$ nanocomposites, compared to that of the pristine $CsPbX_3$ NCs. This blue-shift may result from partial cation exchange between Pb^{2+} and

Zn^{2+}. Similar phenomenon, that is, cation exchange between Pb^{2+} and divalent ions (e.g., Cd^{2+}, Zn^{2+} and Sn^{2+}), has been reported.[44]

It is well-known that whether an ABX_3 perovskite structure can be formed and sustained is predictable by the Goldschmidt tolerance factor,[45]

$$t = (r_A + r_X)/[\sqrt{2}(r_B + r_X)]$$

where r_A, r_B, and r_X are the ionic radii of the respective ions in ABX_3. An ABX_3 perovskite structure is sustainable if the tolerance factor is between 0.8 and 1.1.[46] The tolerance factor of $CsZnBr_3$ is 0.933, which is within the tolerance factor range noted above, to allow for the formation of a stable perovskite structure. Thus, partial cation exchange may occur between Pb^{2+} and Zn^{2+}, leading to a blue-shift of the PL maximum. This can be rationalized as follows. The incorporation of smaller Zn^{2+} results in the contraction of the $PbBr_6$ octahedral, resulting in shorter Pb-Br bonds and thus stronger interactions between the Pb and Br orbitals.[44] As the conduction band minimum is composed of the antibonding combinations between Pb 6p and Br 4p orbitals,[47] it shifts to higher energy with stronger interaction. As a result, the band gap of perovskite NCs increases and their PL maximum blue-shifts. In contrast, for NaSt the tolerance factors of $NaPbBr_3$ and $NaPbI_3$ are 0.752 and 0.749, respectively, which are smaller than 0.8. Consequently, no cation exchange occurs between Na^+ and Cs^+.

Different mass ratios of $CsPbBr_3$ NCs to stearate salts were investigated to examine their influence on the PL spectra. For NaSt and $AlSt_3$, the extent of red-shift in the PL maximum of the resulting nanocomposites decreases as the $CsPbBr_3$ NC/stearate salt mass ratio decreases. As noted above, the red-shift is induced by a closer proximity of perovskite NCs during their impregnation into NaSt and $AlSt_3$. It is not surprising that a lower mass ratio results in a lower concentration of NCs in the stearate matrix, as evidenced in TEM characterizations, which in turn causes a smaller red-shift. For $ZnSt_2$, as the mass ratio increases, the PL maximum of $CsPbBr_3$–$ZnSt_2$ nanocomposites further blue-shifts because more $ZnSt_2$ is introduced, leading to increased cation exchange between Pb^{2+} and Zn^{2+}.

We also studied the effect of solvents (toluene and hexane) used to disperse perovskite NCs during the MSt NC encapsulation process on their PL. The dispersions of pristine $CsPbBr_3$ NCs are also included for comparison. Clearly, $CsPbBr_3$–NaSt and $CsPbBr_3$–$AlSt_3$ nanocomposites display the PL red-shift, regardless of whether toluene or hexane was used. The PL blue-shift can be found for $CsPbBr_3$–$ZnSt_2$ nanocomposites in both toluene and hexane when they are used for $CsPbBr_3$ NCs dispersion. However, the PL blue-shift in toluene is larger than that in hexane. This is because the different solubility of $ZnSt_2$ in toluene and hexane. $ZnSt_2$ is partially dissolved in toluene, thus the cation exchange reaction between $CsPbBr_3$ NCs and $ZnSt_2$ is relatively fast and efficient. In contrast, $ZnSt_2$ cannot be dissolved in hexane, leading to slow and inefficient cation exchange of $CsPbBr_3$ NCs and $ZnSt_2$.

Figure 3 compares the XRD patterns of $CsPbBr_3$ NCs, $CsPbBr_3$–$AlSt_3$ nanocomposites, and pure $AlSt_3$ powders. All diffraction peaks of $CsPbBr_3$ NCs can be readily identified in the XRD spectrum of $CsPbBr_3$–$AlSt_3$ nanocomposites, signifying that the crystal structures of $CsPbBr_3$ NCs are retained in nanocomposites. Specifically, $CsPbBr_3$–$AlSt_3$ nanocomposites have the diffraction peaks at 2theta of 15.1°, 21.4° and 30.4°, corresponding to the (100), (110) and (200) crystalline planes of $CsPbBr_3$ NCs. While the diffraction peaks at 2theta of 6.7°, 11.5°, 19.5° and 23.2° are from the $AlSt_3$ matrix. Clearly, these results suggest that the cubic structure of $CsPbBr_3$ NCs is

well preserved after the impregnation of $CsPbBr_3$ NCs in the $AlSt_3$ matrix. We note that the peak intensities from $CsPbBr_3$ are relatively weak compared to those of $AlSt_3$ as the latter is the matrix.

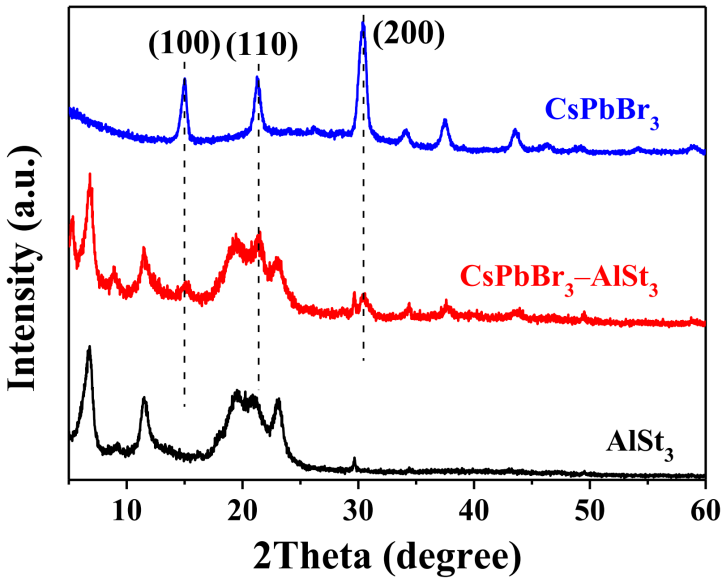

Figure 3. XRD patterns of $CsPbBr_3$–$AlSt_3$ nanocomposites (red curve), $CsPbBr_3$ NCs (blue curve) and pure $AlSt_3$ (black curve).

To investigate the interaction between $CsPbBr_3$ and $AlSt_3$ in nanocomposites, FTIR and XPS studies were performed. **Figure 4** depicts the FTIR analysis of $CsPbBr_3$ NCs and $CsPbBr_3$–$AlSt_3$ nanocomposites with different $CsPbBr_3/AlSt_3$ ratios. For $CsPbBr_3$ NCs, the stretching vibrations of N-H at 3030 cm^{-1}, C-H at 2925 cm^{-1} and 2854 cm^{-1}, C=C at 1608 cm^{-1} and C-N at 1382 cm^{-1} as well as the bending vibration of C=C at 908 cm^{-1} are observed, revealing the presence of surface capping ligands (i.e., OLA). In contrast, FTIR spectra of nanocomposites show the disappearance of N-H, C=C and C-N vibrations, indicating the absence of OLA. The vibrations of $CsPbBr_3$–$AlSt_3$ nanocomposites are at the same wavenumbers as those of $AlSt_3$, representing the presence of $AlSt_3$. Moreover, XPS studies of O 1s, C 1s and N 1s are observed, where both O 1s and C 1s peaks shift to larger binding energies after the impregnation of $CsPbBr_3$ NCs in $AlSt_3$. N 1s peaks can be clearly observed in $CsPbBr_3$ NCs, while they cannot be detected in $CsPbBr_3$–$AlSt_3$ nanocomposites, suggesting the absence of OLA in $CsPbBr_3$–$AlSt_3$ nanocomposites. These results suggest that during the co-precipitation process the original OLA ligands on the surface of $CsPbBr_3$ NCs were exchanged by $AlSt_3$ as discussed in the mechanism above, confirming a stable perovskite-$AlSt_3$ nanocomposite powder phosphor system for SSL application.

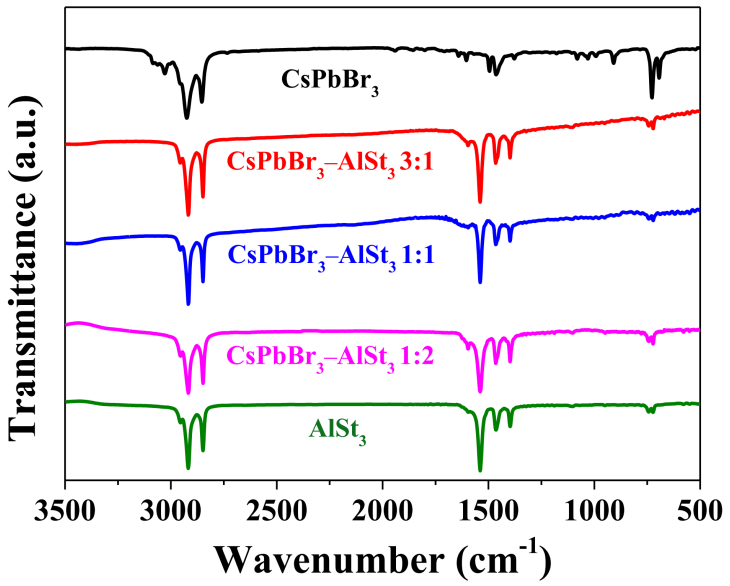

Figure 4. FTIR spectra of $CsPbBr_3$ NCs and $CsPbBr_3$–$AlSt_3$ nanocomposites with varied mass ratios ($CsPbBr_3/AlSt_3$ = 3:1, 1:1, 1:2). FTIR spectrum of pure $AlSt_3$ is also included as the reference.

XPS studies revealed that after encapsulation by $AlSt_3$, Cs 3d, Pb 4f, Br 3d peaks all shifted to the larger binding energies, particularly Pb 4f and Br 4d peaks (**Figure 5**). This may suggest the coordination bond of St–Cs and St–Pb as well as an ionic bond between metal ions from MSt and X^- on the surface of $CsPbX_3$. On the basis of XPS and FTIR measurements, we propose a plausible mechanism of the $AlSt_3$ encapsulation for yielding $CsPbBr_3$–$AlSt_3$ nanocomposites. In the presence of $AlSt_3$, the weakly bound surface ligands OLA are exchanged by $AlSt_3$. As a result, Al^{3+} preferentially adsorbs to the surface of NCs via Al^{3+}–Br^- interaction, accompanied by long St chain situating on the surface of NCs or coordinating with Cs^+ and Pb^{2+} of NCs. Similar ligand-dependent colloidal stability has been reported in CdSe NCs [48]. For the saturated solution of CdSe NCs, a dramatically decreased solubility was observed as the length of n-alkanoate ligands change from C_{14} to C_{22}, which was ascribed to the increased van der Waals attraction of NCs via the ligand interdigitation between neighboring NCs.

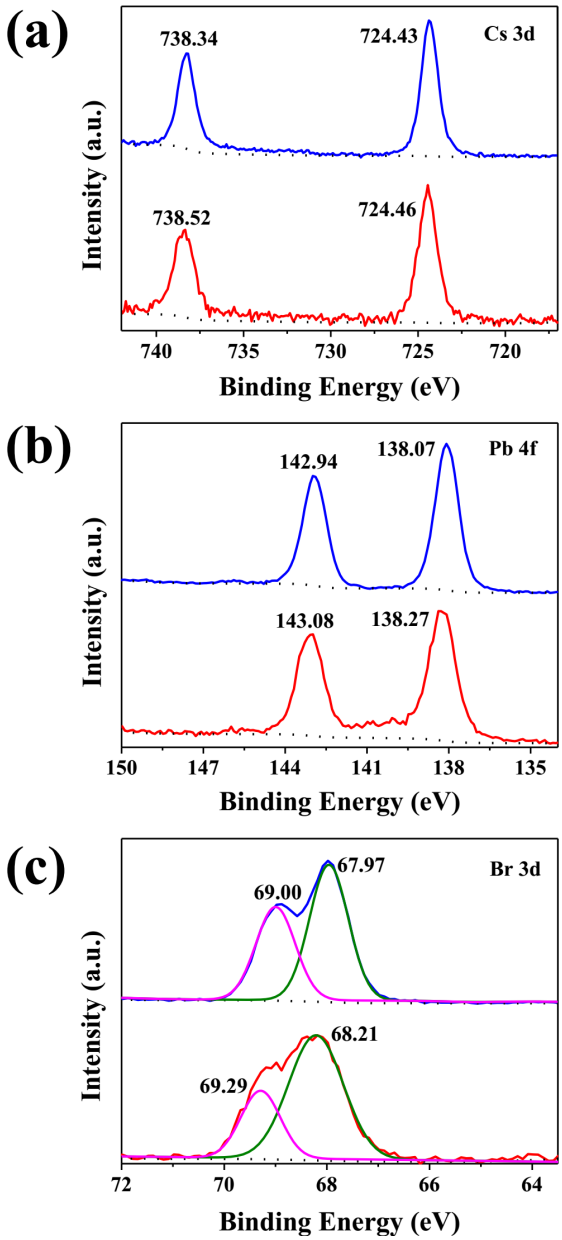

Figure 5. High resolution XPS spectra of Cs 3d, Pb 4f, and Br 3d in $CsPbBr_3$ NCs (upper blue curves) and $CsPbBr_3$–$AlSt_3$ nanocomposites (lower red curves). (a) Cs 3d. (b) Pb 4f. (c) Br 3d, where the fitted curves are shown in purple and green.

The PL lifetime of $CsPbBr_3$ NCs and $CsPbBr_3$–$AlSt_3$ nanocomposites were studied as well. $CsPbBr_3$–$AlSt_3$ nanocomposites possess longer lifetimes than those of $CsPbBr_3$ NCs, which can be ascribed to the surface passivation of $AlSt_3$.

In the work that follows, we demonstrate an impressive set of excellent stabilities, as required for an effective SSL NC phosphor system, that $CsPbX_3$–MSt nanocomposites carry, including water stability, compositional stability, phase stability, and phase segregation stability. First, we take $CsPbBr_3$–$AlSt_3$ nanocomposites as an example to showcase high water resistance of

$CsPbX_3$–MSt nanocomposites (**Figure 6b**). Sonication was applied to assist in the homogeneous mixing between liquid/liquid (water/toluene) and liquid/solid (water/nanocomposites) phases. For $CsPbBr_3$ NCs in toluene, after addition of water followed by sonication, the solution emission becomes weaker and completely disappears after 25 min (**Figure 6a**). In stark contrast, after sonication for 25 min $CsPbBr_3$–$AlSt_3$ nanocomposites still display bright PL and remain highly luminescent even after being stored overnight (**Figure 6b**). This observation clearly indicates the prominent water resistance of $CsPbBr_3$–$AlSt_3$ nanocomposites, suggesting the effective encapsulation and protection of $CsPbBr_3$ NCs by $AlSt_3$ matrix.

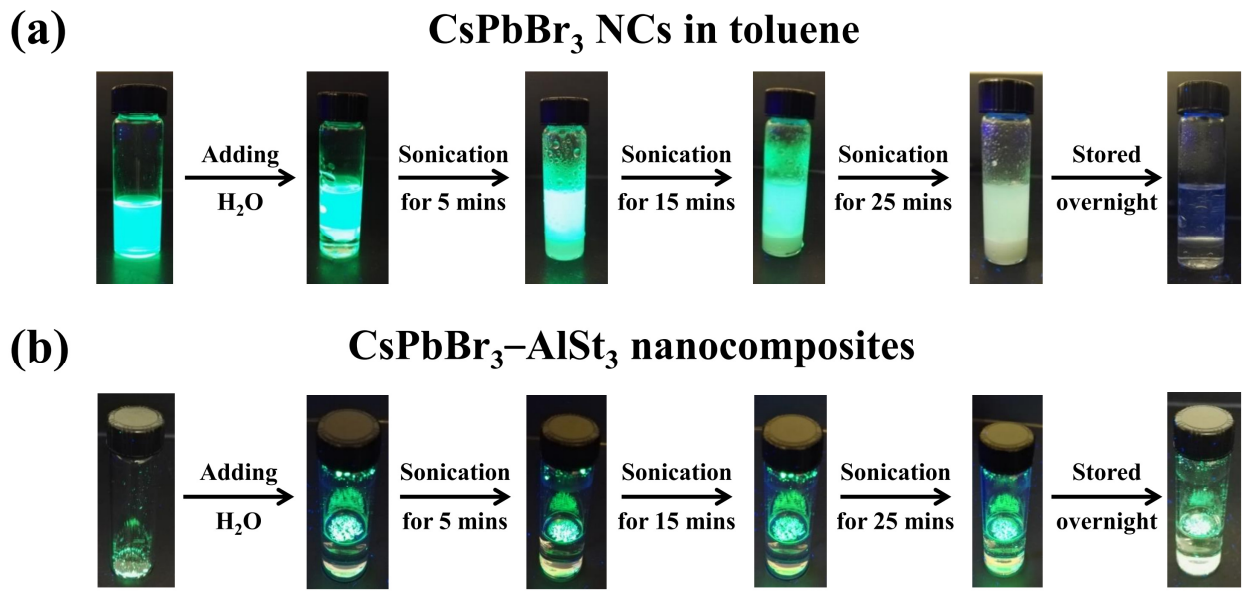

Figure 6. Digital images of (a) $CsPbBr_3$ NCs in toluene and (b) $CsPbBr_3$–$AlSt_3$ nanocomposites exposed to 365 nm UV light after the addition of water, sonication for different times, and stored overnight.

The compositional stability (i.e., anion exchange stability) of $CsPbX_3$–MSt nanocomposites was then evaluated. As shown in **Figure 7a**, immediately after mixing $CsPbBr_3$ and $CsPbI_3$ NC powders together, the two PL peaks merge into a broadened peak (Mixture 1) with much reduced intensity composed of several subpeaks situated between the original $CsPbBr_3$ and $CsPbI_3$ PL emissions due to the partial anion exchange between Br^- and I^-.[28,36] After 1 h, these broad PL peaks merge into a narrow single peak (Mixture 2 in **Figure 7a**), signifying the complete anion exchange.[28] Taking the mixing of $CsPbBr_3$–$AlSt_3$ and $CsPbI_3$–$AlSt_3$ nanocomposites as an example, it is notable that there were no salient PL peak positions and intensity changes even after mixing these two nanocomposites for 1 day. Clearly, these results corroborate that $CsPbBr_3$ and $CsPbI_3$ NCs encapsulated within the respective $AlSt_3$ matrix are well protected and effectively isolated from each other preventing them from anion exchange.

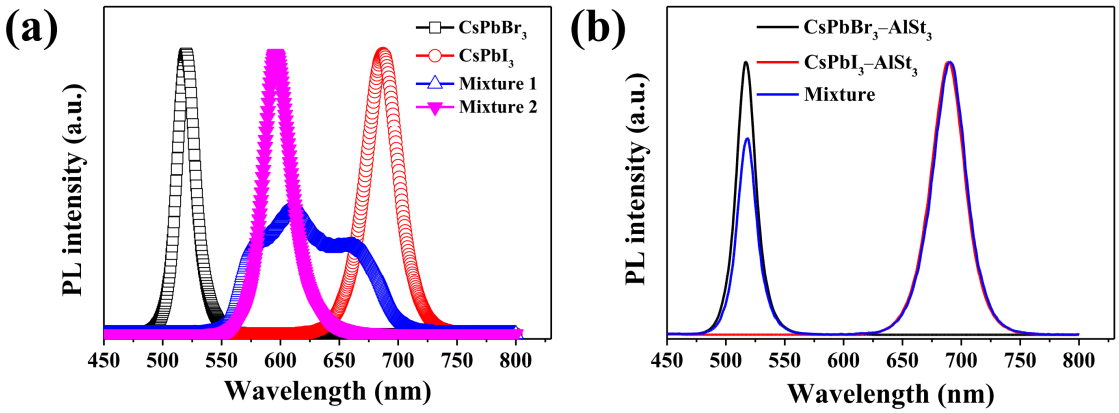

Figure 7. (a) PL spectra of $CsPbBr_3$ NC powders, $CsPbI_3$ NC powders, and their mixtures (mixture 1 taken after mixing for 5 min, and mixture 2 taken after mixing for 1h). (b) PL spectra of $CsPbBr_3$–$AlSt_3$ nanocomposites, $CsPbI_3$–$AlSt_3$ nanocomposites, and their mixture after mixing for 1 day.

As for phase stability of nanocomposites, $CsPbI_3$–$AlSt_3$ was used as an example. We first investigated their PL under ambient condition. For comparison, the PL of $CsPbI_3$ NCs was also measured. **Figure 8a** shows the PL intensity of $CsPbI_3$ NCs in toluene drops quickly within 10 days. The XRD measurements clearly suggest the phase transition of $CsPbI_3$ NCs. The freshly synthesized $CsPbI_3$ NCs have cubic phase and transform into orthorhombic phase after 10 days. In sharp contrast, the $CsPbI_3$–$AlSt_3$ nanocomposites still maintain 85 % of the original PL intensity after 30 days (**Figure 8b**). Moreover, no orthorhombic phase can be found in the XRD pattern of nanocomposites after 30 days (**Figure 8d**), which is comparable to those reported in literature. These results demonstrate that the passivation of $CsPbI_3$ NCs with $AlSt_3$ is highly effective and greatly suppresses the phase transformation of $CsPbI_3$ NCs from emissive cubic phase to non-emissive orthorhombic phase. There are two reasons which may account for the phase stability of $CsPbI_3$ NCs after impregnation in $AlSt_3$. First, $AlSt_3$ can effectively isolate $CsPbI_3$ NCs from the surrounding environment containing moisture and oxygen that accelerate the phase transition of $CsPbI_3$ NCs from cubic to orthorhombic. Second, $AlSt_3$ may release the lattice strain which is the driving force for phase transition of $CsPbI_3$ NCs. Notably, it has been reported that the lattice strain causes the intrinsic instability of the cubic phase at ambient temperature, and drives the phase transformation into the orthorhombic phase.[22,34] Similar phase stability was also found in $CsPbI_3$–NaSt and $CsPbI_3$–$ZnSt_2$ nanocomposites. Both $CsPbI_3$–NaSt and $CsPbI_3$–$ZnSt_2$ nanocomposites display high PL intensity after 30 days.

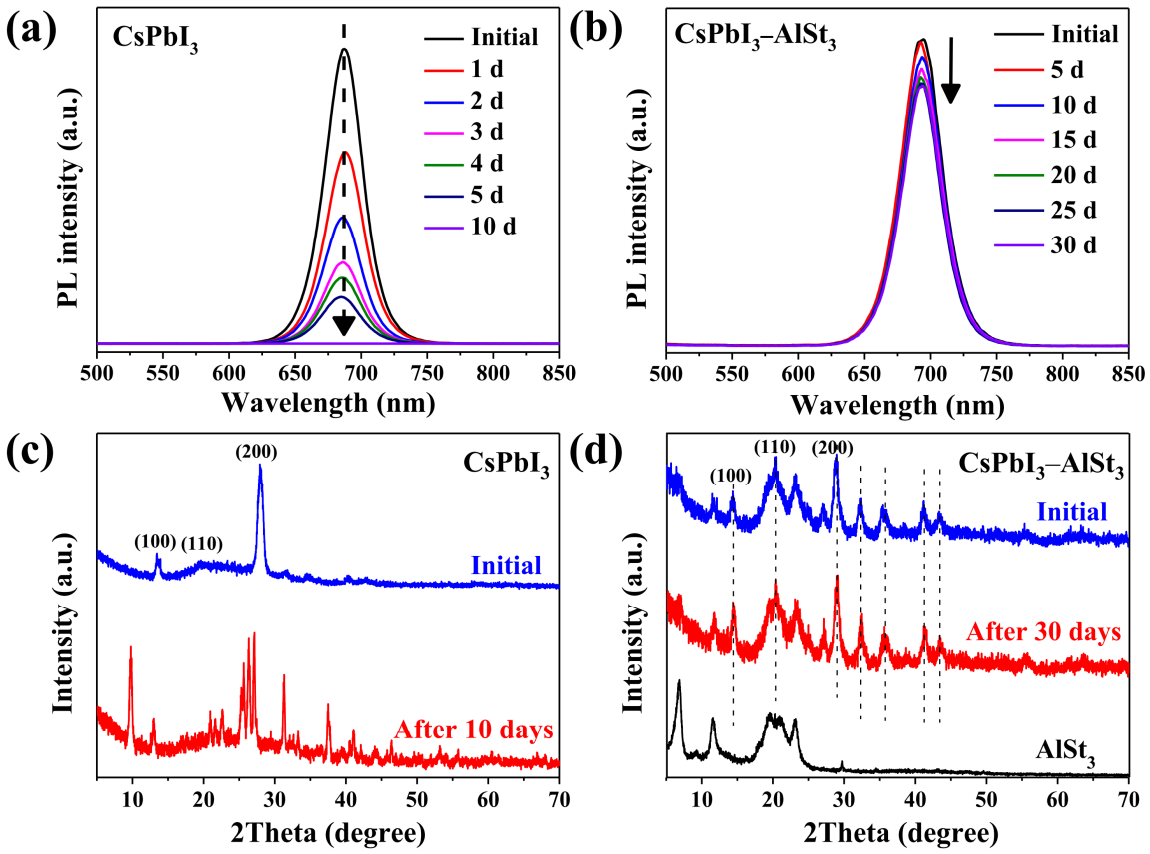

Figure 8. PL evolutions of (a) $CsPbI_3$ NCs dispersed in toluene, and (b), $CsPbI_3$–$AlSt_3$ nanocomposites in solid state under ambient condition. The corresponding XRD patterns of (c) $CsPbI_3$ NCs before (blue line) and after (red line) being stored under ambient condition for 10 days (dry state), and (d) $CsPbI_3$–$AlSt_3$ nanocomposites before (blue line) and after (red line) being stored under ambient condition for 30 days (dry state). XRD pattern of $AlSt_3$ (black line) is also provided as the reference.

Notably, as-prepared nanocomposites also possess remarkable phase segregation stability. In this regard, $CsPbBr_{1.5}I_{1.5}$ NCs and $CsPbBr_{1.5}I_{1.5}$–$AlSt_3$ nanocomposites were examined and compared, revealing that $AlSt_3$ impregnation can effectively prevent phase segregation and retain their structural stability. **Figure 9a** depicts that within 20 days the PL intensity of $CsPbBr_{1.5}I_{1.5}$ NCs drops quickly and the PL maximum blue-shifts largely, which is consistent with the previous report in literature.[49] By contrast, after $AlSt_3$ encapsulation, there is only a slight decrease in PL intensity of $CsPbBr_{1.5}I_{1.5}$–$AlSt_3$ nanocomposites. No detectable PL peak shift can be observed, suggesting no phase segregation (i.e., forming the respective $CsPbBr_3$ and $CsPbI_3$; **Figure 9b**). This is also probably due to the fact that $AlSt_3$ encapsulation offsets lattice strain which improves the phase stability. These results clearly indicate that the $AlSt_3$ encapsulation is robust and prevents the phase segregation of mixed-halide perovskite.

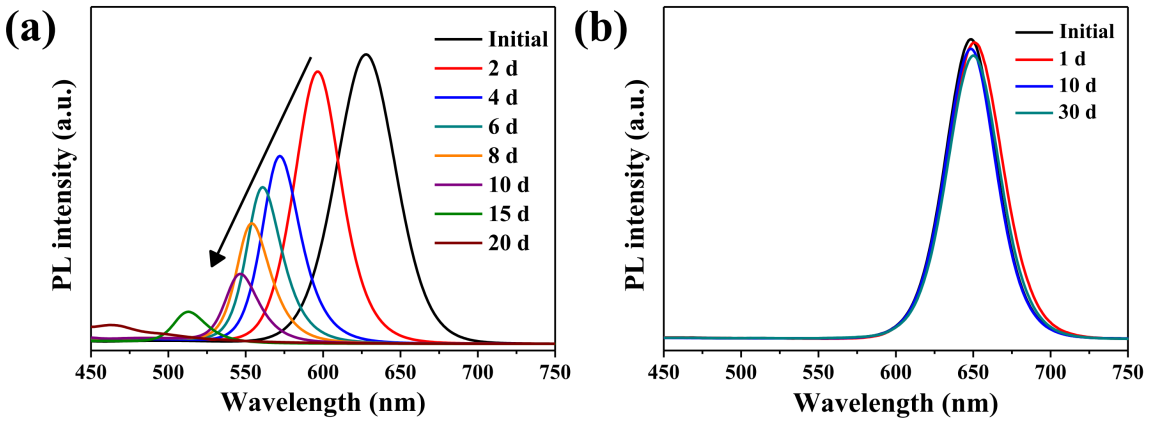

Figure 9. PL evolutions of (a) $CsPbBr_{1.5}I_{1.5}$ NCs dispersed in toluene, and (b), $CsPbBr_{1.5}I_{1.5}$–$AlSt_3$ nanocomposites in solid state under ambient condition.

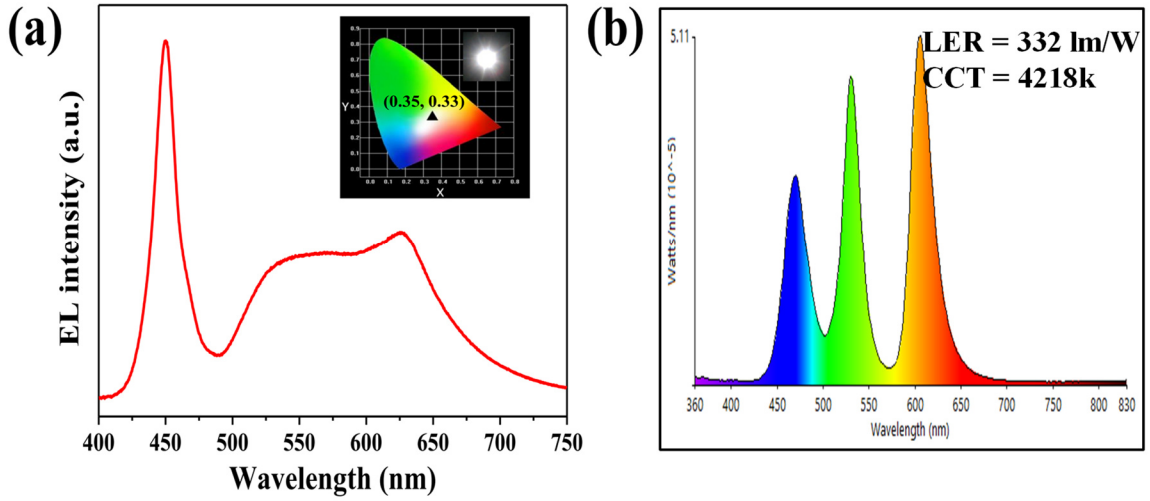

Figure 10. (a) Emission spectrum and CIE color coordinate of WLED crafted by depositing a mixture of YAG: Ce^{3+} and $CsPbBr_{1.5}I_{1.5}$–$AlSt_3$ nanocomposites on a blue InGaN chip. Inset: WLED operated under 30 mA driven current. (b) Emission spectrum of *RadiantFlex* screen composed of green and red-emitting perovskite-AlSt3 nanocomposites with LER=332 lm/W under blue LED excitation.

As described above, $CsPbX_3$–MSt nanocomposites exhibit a suite of excellent stabilities. Subsequently, WLEDs and RadiantFlex sheets composed of $CsPbX_3$-MSt nanocomposites was assembled. Commercially available WLEDs usually involve the use of a blue-emitting InGaN chip as the excitation source and YAG:Ce yellow phosphors as the color conversion layer. However, such kind of WLEDs suffer from low CRI (<80) as YAG:Ce phosphors are lack of red-spectrum emission. **Figure 10a** shows the emission spectrum of a WLED constructed using the mixture of YAG:Ce phosphors and $CsPbBr_{1.5}I_{1.5}$-$AlSt_3$ nanocomposites. Bright and warm white light is emitted with a high CRI of 89.9 at a CCT of 4588 K, and a CIE color coordinate of (0.35, 0.33) under 30 mA driven current, signifying the great potential of $CsPbX_3$-MSt nanocomposites for use

as solid-state luminophores in WLEDs. **Figure 10b** shows emission spectrum of a *RadiantFlex* screen composed of green and red-emitting perovskite-AlSt3 nanocomposites with LER of 332 lm/W and CCT of 4218k under blue LED excitation.

Experimental Methods

Preparation of Cs-oleate

Cs-oleate was prepared by following a previously reported procedure.[32] Cs_2CO_3 (0.8 g), OA (2.5 mL) and ODE (30 mL) were added into a 100 mL 3-neck flask and degassed for 1 h at 120 ºC, and then heated to 150 ºC under flowing N_2 until the solution turned clear. We note that the Cs-oleate ODE solution has to be pre-heated to 100 ºC prior to injection to the PbX_2 ODE solution as Cs-oleate precipitates out of ODE at room temperature.

Synthesis of $CsPbX_3$ NCs

ODE (5 mL) and PbX_2 (0.188 mmol; i.e., PbI_2 (0.087 g), $PbBr_2$ (0.069 g), or a mixture of PbI_2 (0.0435 g) and $PbBr_2$ (0.0345 g)) were added into a 25 mL 3-neck flask and degassed for 1 h at 120 ºC. Dried OLA (0.5 mL) and OA (0.5 mL) were injected into the PbX_2 ODE solution at 120 ºC under N_2. After the solution turned clear, the temperature was raised to 120~160 ºC and Cs-oleate solution (0.4 mL) was quickly introduced, and, 5 s later, the reaction mixture was cooled by ice-water bath.

Impregnation of $CsPbX_3$ NCs within metal stearates (MSt)

Crude solution of as-synthesized $CsPbX_3$ NCs was dissolved in toluene, and centrifuged at 6500 rpm for 10 min. The supernatant was discarded and the precipitation was re-dispersed in toluene and centrifuged at 6500 rpm for 10 min. Then, the precipitate was discarded and 50 mg MSt was added to the supernatant (25 mg/mL) under vigorous stirring. The MSt used in this work includes aluminum stearate ($AlSt_3$), zinc stearate ($ZnSt_2$), and sodium stearate (NaSt). After 10 min, the stirring was stopped and the mixed solution was allowed to precipitate. After centrifugation at 5000 rpm for 5 min, the supernatant was discarded while the precipitate was dried in an oven at 60 ºC overnight.

Fabrication of WLED

Typically, epoxy resin was used as the encapsulating material in the packaging of LEDs. Equal amounts of transparent epoxy JH-6800MA and JH-6800MB were mixed together, after which cerium-doped yttrium aluminum garnet (YAG: Ce^{3+}) phosphors and as-prepared $CsPbBr_{1.5}I_{1.5}$ NCs-$AlSt_3$ nanocomposites were added. The mixture was stirred thoroughly and then dispersed on a InGaN LED chip. The coated WLED chip was solidified in an oven at 80 ºC for 2 h.

2. Stability enhancement of perovskite NCs at single particle level via permanently ligating with polymer hair

Figure 11 depicts the synthetic route to hairy all-inorganic perovskite NCs intimately and permanently ligated by PS chains via capitalizing on amphiphilic unimolecular star-like PAA-*b*-PS diblock copolymers as nanoreactors, where the formation of $CsPbBr_3$ NC is taken as an example.

First, a series of star-like poly(*tert*-butyl acrylate)-*block*-polystyrene (denoted P*t*BA-*b*-PS; upper right panel in **Figure 11**) diblock copolymers with precisely controlled molecular weight and low polydispersity of the inner P*t*BA and outer PS blocks were synthesized via sequential ATRP of *tert*-butyl acrylate (*t*BA) and styrene (St) monomers using 21-Br-β-CD as a macroinitiator (see *Experimental Section*).[50-59] Subseqeuently, the inner P*t*BA blocks were hydrolyzed into PAA blocks, resulting in amphiphilic unimolecular star-like PAA-*b*-PS (lower right panel in **Figure 11**). Notably, in contrast to conventional linear block copolymer micelles formed by much weaker forces of attraction,[60] there are 21 arms of PAA-*b*-PS diblock copolymer anchored covalently to a single macroinitiator. The molecular weights of star-like PAA-*b*-PS characterized by GPC and ^{1}H-NMR spectra are summarized in **Table 1**.

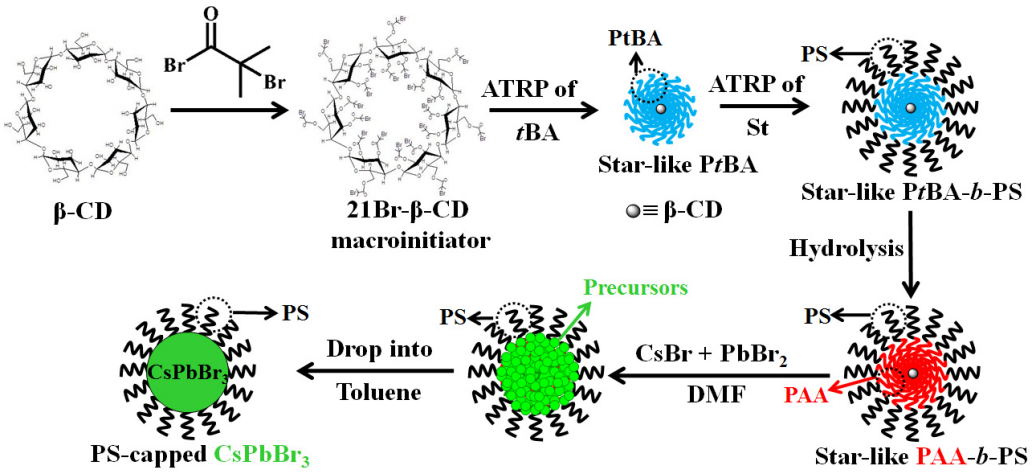

Figure 11. Schematic stepwise representation of crafting hairy all-inorganic perovskite $CsPbBr_3$ NCs intimately and permanetnly capped by PS chains via capitalizing on amphiphilic star-like PAA-*b*-PS diblock copolymer as nanoreactor. Star-like all hydrophobic P*t*BA-*b*-PS diblock copolymer is syntheisezed via sequential atom transfer radical polymerization of tert-butylacrylate (*t*BA) and styrene (St) using 21Br-β-CD as macroinitiator. Hydrolysis of star-like P*t*BA-*b*-PS yields amphiphilic star-like PAA-*b*-PS. Perovskite precursors of CsBr and $PbBr_2$ are selectively partitioned in the compartment occupied by hydrophilic PAA blocks. Co-precipetation of CsBr and $PbBr_2$ in nonpolar solvent (e.g., toluene) leads to the formation of green-emitting PS-capped $CsPbBr_3$ NCs.

Amphiphilic star-like PAA-*b*-PS diblock copolymers were then exploited as nanoreactors to template the synthesis of $CsPbBr_3$ NCs tethered by PS chains that were originally covalently bonded to PAA chains. First, the star-like nanoreactor, cesium bromide (CsBr), and lead bromide ($PbBr_2$) were fully dissolved in anhydrous N,N-dimethylformamide (DMF). The perovskite ions selectively occupied the inner PAA-containing compartment of the nanoreactor by strongly coordinating with the carboxyl groups of the inner PAA blocks (i.e., forming the CsBr- and $PbBr_2$-loaded nanoreactor solution; lower central panel in **Figure 11**).[52,57,61,62] Subsequently, by dropping the solution into a poor solvent (i.e., toluene) for the perovskite precursors, $CsPbBr_3$ NCs were rapidly produced via co-precipitation[63] in toluene (lower left panel in **Figure 11**), selectively confined within the inner PAA compartment. This is not surprising as perovskite NCs would otherwise be decomposed in DMF due to their ionic nature. It is worth noting that as PS dissolves well in toluene, the aggregation of PS-capped perovskite NCs in toluene was thus prevented.

Table 1. Molecular weights of amphiphilic star-like PAA-*b*-PS diblock copolymers

Nanoreactor	$M_{n,PAA}$[a] (kg/mol)	$M_{n,PS}$[b] (kg/mol)
Star-like PAA-*b*-PS Sample 1	5.1	8.5
Star-like PAA-*b*-PS Sample 2	5.1	16.9
Star-like PAA-*b*-PS Sample 3	7.8	9.6
Star-like PAA-*b*-PS Sample 4	7.8	13.2
Star-like PAA-*b*-PS Sample 5	11.0	7.3
Star-like PAA-*b*-PS Sample 6	11.0	16.4

Notes: [a]M_n of each PAA block arm calculated from the molecular weight difference between the PtBA block (before hydrolysis) and PAA block (after hydrolysis). [b]Mn of each PS block arm calculated from ^{1}H-NMR.

Figure 12 compares the synthesis of $CsPbBr_3$ NCs by capitalizing on star-like PAA-*b*-PS nanoreactors (i.e., sample 5 in **Table 1**; where the molecular weight of a single PS chain is 7300 g/mol, thus the resulting NCs are referred to as PS(7k)-capped $CsPbBr_3$ NCs) and by utilizing oleic acid as the common linear ligand, respectively. For both systems, the precursor solution contains the same molar content of all reactants, and the reaction was conducted by adding the nonpolar solvent toluene to co-precipitate two precursors (i.e., CsBr and $PbBr_2$) at room temperature. For the PS(7k)-capped $CsPbBr_3$ NCs, as the precursor solution was dropped into toluene, co-precipitation of CsBr and $PbBr_2$ occurred selectively within the inner PAA compartment of the star-like PAA-*b*-PS nanoreactor. Due to hydrophobic PS capping, green-emitting NCs rapidly formed in the solution in less than 1 sec (**Figure 12a**), suggesting the homogeneous dispersion of NCs in toluene.

In contrast, $CsPbBr_3$ capped with oleic acid (see *Experimental Section*; **Figure 12b**) and $CsPbBr_3$ with no ligands present (see *Experimental Section*) were initially bright when toluene was added into the precursor solution; however, the photoluminescence (PL) of $CsPbBr_3$ quickly disappeared (< 1 sec) due to aggregation of NCs as a result of weak binding of oleic acid to NC at room temperature. Notably, it has been reported that high-temperature hot-injection of precursors in the presence of oleic acid produces relatively stable $CsPbBr_3$ NCs,[64] due likely to the improved binding between oleic acid and NCs The observations noted above were verified by TEM measurements, where uniform PS(7k)-capped $CsPbBr_3$ NCs with an average size of 13.9±0.7 nm were seen (size distribution within 5% of average size, which can be regarded as monodisperse; **Figure 12c**), while aggregates of $CsPbBr_3$ was found for the oleic acid and no ligand samples (**Figure 12d**). The HRTEM studies (inset in **Figure 12c**) reveal that PS(7k)-capped $CsPbBr_3$ NC is highly crystalline. Clearly, the ability to craft uniform PS(7k)-capped $CsPbBr_3$ NCs demonstrates the effectiveness of star-like nanoreactor in synthesizing high-quality hairy $CsPbBr_3$ NCs.

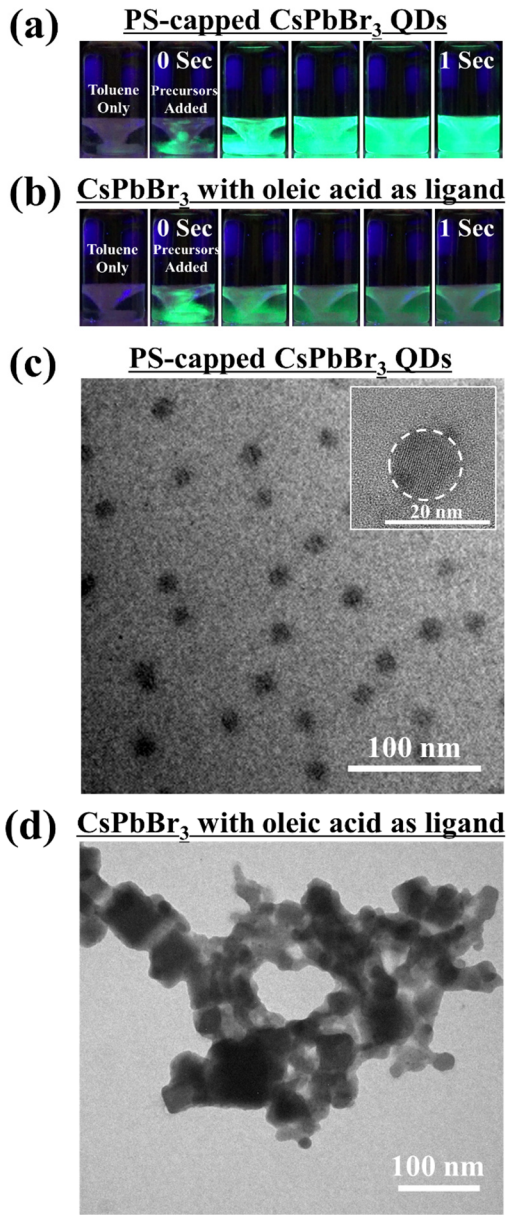

Figure 12. Synthesis of $CsPbBr_3$ with and without the use of star-like PAA-*b*-PS diblock copolymers as nanoreactors. Digital images displaying the rapid formation process of (a) PS-capped $CsPbBr_3$ NCs (capitalizing on star-like PAA-*b*-PS nanoreactors; sample 5 in **Table 1**), and (b) $CsPbBr_3$ (using oleic acid as ligand only; in the absence of star-like PAA-*b*-PS), by adding the precursors-containing (i.e., CsBr and $PbBr_2$) DMF solution into toluene (i.e. a co-precipitation approach) over 1 sec at room temperature. TEM images of (c) PS-capped $CsPbBr_3$ NCs corresponding to the sample synthesized in (a) (average diameter, D = 13.9±0.7 nm), and (d) aggregated $CsPbBr_3$ nanocrystals corresponding to the sample produced in (b).

Successful synthesis of green-emitting $CsPbBr_3$ NCs was further substantiated by absorption, PL and XRD measurements (**Figure 13**). PS(7k)-capped $CsPbBr_3$ NCs display the first exciton absorption peak at 503 nm and PL peak at 516 nm, which agrees well with conventional $CsPbBr_3$

NCs prepared by other methods (e.g., hot-injection).[11] It is interesting to note that the FWHM, and indirect measure of the monodispersity of NCs, is as low as 17.7 nm for PS(7k)-capped $CsPbBr_3$ NCs, which is comparable to the lowest value for $CsPbBr_3$ NCs reported,[65] leading to superior color quality for display backlight applications compared to currently used CdSe/ZnS NCs (FWHM ~30nm). The XRD diffraction peaks also coincide well with the monoclinic phase $CsPbBr_3$ (PDF#18-0364) observed for $CsPbBr_3$ NCs synthesized via the co-precipitation method described in literature.[63]

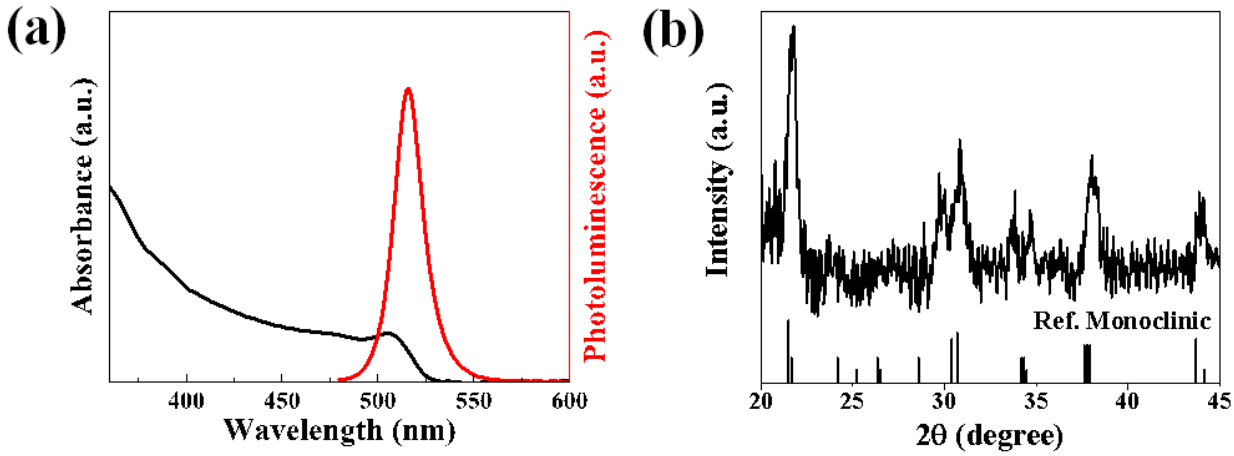

Figure 13. Characterization of PS(7k)-capped $CsPbBr_3$ NCs. (a) Absorption and photoluminescence (PL) spectra of PS(7k)-capped $CsPbBr_3$ NCs, where the absorption and PL maxima are 503 nm and 516 nm, respectively. (b) XRD pattern of PS(7k)-capped $CsPbBr_3$ NCs crafted by employing star-like PAA-*b*-PS diblock copolymers (i.e., sample 5 in **Table 1**) as nanoreactors.

Anion exchange of the Br^- group in PS-capped $CsPbBr_3$ NCs using $ZnCl_2$ and ZnI_2[29] was then performed to yield blue-emitting $CsPbCl_3$ and red-emitting $CsPbI_3$ NCs (**Figure 14a**) with their PL peak positions blue-shifted to 427 nm and red-shifted to 700 nm, respectively (**Figure 14b**). The anion exchange process was proceeded by first dissolving zinc halide (ZnX_2) in methanol, followed by dropping the solution into as-synthesized PS-capped $CsPbBr_3$ NC solution (**Figure 14c**). Notably, as polar solvents such as methanol are known to be detrimental to perovskites, a control experiment was conducted in which the same amount of ZnI_2 in two different volumes of methanol was added. The results showed that small amounts of methanol ($\leq$ 60 μl) did not have any effect in changing the PL peak position, signifying the reliability of anion exchange in fine-tuning the composition of PS-capped perovskite NCs. Subsequently, the overall iodide amount dropped into the NC solution was controlled to modulate the PL peak position while the methanol amount was kept constant. As more iodide was added into the NC solution, a steady red-shift in the PL peak position was observed. To verify the reproducibility of the anion exchange process, each anion exchange experiment was repeated once, and the results showed that for three different compositions, the PL spectra overlapped well between each trial.

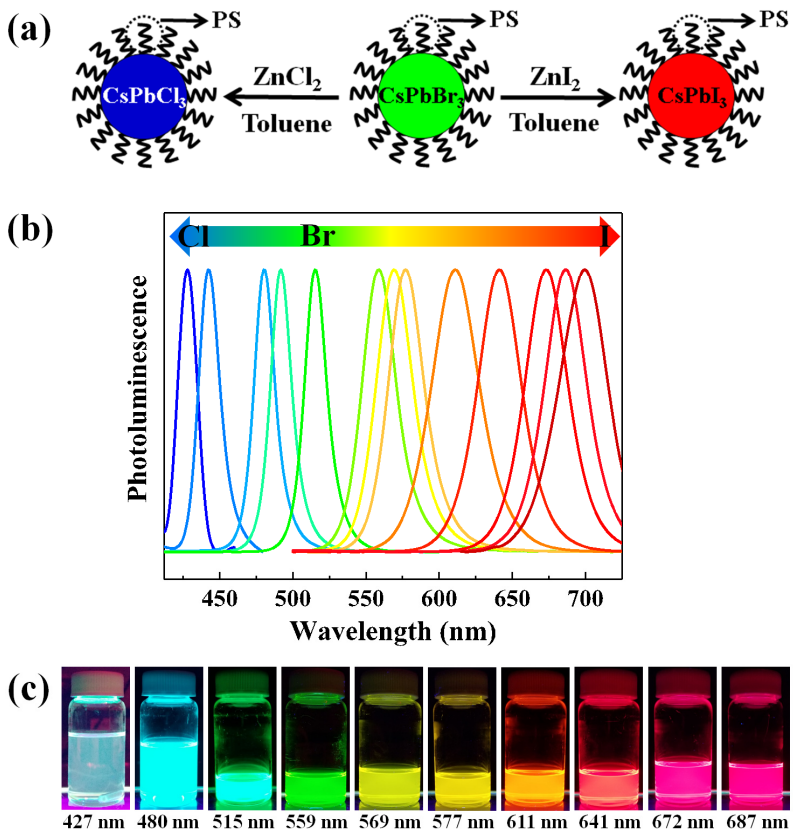

Figure 14. Control over optical properties of PS-capped perovskite $CsPbBr_3$ NCs crafted using star-like PAA-*b*-PS diblock copolymers (i.e., sample 5 in Table 1) as nanoreactors via anion exchange with zinc halide (i.e., $ZnCl_2$ and ZnI_2). (a) Schematic displaying synthetic route to PS-capped $CsPbCl_3$ NCs and PS-capped $CsPbI_3$ NCs via anion exchange with $ZnCl_2$ and ZnI_2, respectively. (b) Photoluminescence (PL) spectra and (c) digital images of a series of representative PS-capped perovskite NCs under UV excitation, where the contents of Cl and I in NCs are progressively varied, exhibiting systematic color change from green ($CsPbBr_3$) to blue ($CsPbCl_3$) as well as to red ($CsPbI_3$).

As ZnX_2 does not dissolve well in non-polar solvents such as toluene, there was a possibility that ZnX_2 in methanol can aggregate (i.e., precipitate) the PS-capped perovskite NCs during its addition to the NC toluene solution. However, TEM imaging on anion-exchanged PS-capped perovskite NCs shows that there was neither aggregation nor shape change of NCs caused by the anion exchange process, signifying that anion exchange via ZnX_2 is a viable approach for tailoring the PL emission wavelength for PS-capped perovskite NCs. The stability of anion-exchanged NCs was also confirmed by the retention of PL emission under UV excitation after storing the NC solution under ambient condition for 3 weeks, where no noticeable decrease in PL was found.

In addition to the composition-dependent tuning of optical properties as noted above, remarkably, the star-like block copolymer nanoreactor strategy can also effectively alter the size of NCs to manipulate their optical properties. By synthesizing the star-like diblock copolymer with precisely controlled length (i.e., molecular weight) of each block and low polydispersity via ATRP, the size of perovskite NCs can be accurately regulated (**Figure 15a**), thereby rendering strict

control over light harvesting and emission of NCs at desired wavelengths in the visible region (**Figure 15b-15d**). The molecular weights and polydispersity index (PDI) of a series of star-like PAA-*b*-PS nanoreactors are summarized in **Table 1**. The size of the three PS-capped $CsPbBr_3$ NCs crafted are 8.6±0.3 nm, 10.1±0.6 nm, 13.9±0.7 nm, and their corresponding PL peaks are at 514 nm, 515 nm, and 516 nm, respectively (**Figure 15b**). It is notable that as the sizes of these crafted NCs are above the Bohr diameter of $CsPbBr_3$ NC of 7 nm,[11] the PL peak position change is minimal. In contrast, for PS-capped $CsPb(Br_{0.1}I_{0.9})_3$ synthesized by partial anion exchange of $CsPbBr_3$ with ZnI_2 as descried above, which has a Bohr diameter of nearly 12 nm,[11] the PL peak positions are more distinctly separated at 685 nm, 695 nm, and 698 nm, respectively (**Figure 15c**), clearly displaying the quantum confinement effect (**Figure 15d**). All these PS-capped $CsPbBr_3$ NCs (D = 13.9 nm, 10.1 nm, and 8.6 nm) are crystalline as revealed by HRTEM (lower panels in **Figure 15a**). The green-emitting PS-capped $CsPbBr_3$ NCs (D = 13.9 nm) exhibited a high PL quantum yield (QY) of 69% and a FWHM as low as 17.7 nm. As the size of the PS-capped $CsPbBr_3$ NCs decreased, the QY decreased to 67% (D =10.1 nm) and 38% (D = 8.6 nm), which may be due to the higher weight fraction of PAA groups in smaller PS-capped $CsPbBr_3$ NCs and large surface-to-volume ratio of smaller-sized NCs that may possess higher density of surface defects.[66,67] It should be noted that despite the existence of PAA chains within $CsPbBr_3$ NCs and the lack of an inorganic shell as in the core/shell NCs to reduce surface detects, the high QY observed in $CsPbBr_3$ NCs is due largely to the high defect-tolerance characteristic of perovskite material as a result of its unique band structure and optical properties.[68] The valence band maximum (VBM) of perovskite is antibonding in nature and the conduction band minimum (CBM) is stabilized by strong spin−orbit coupling, as opposed to common II−VI and III−V NCs wherein VBM is constituted by bonding orbitals. [68]

To further corroborate the effectiveness of star-like nanoreactors in fine-tuning NC size through the precise tailoring of the inner PAA block length, the characteristic time-resolved PL (TRPL) decay lifetime as a function of NC size was also measured (see *Experimental Section*; **Figure 15e**). The TRPL decay curves were best-fit using a biexponential decay function:

$$A(t) = A_1 exp\left(-\frac{t}{\tau_1}\right) + A_2 exp\left(-\frac{t}{\tau_2}\right)$$

where A, A_1, and A_2 are constants; t is time; τ_1 and τ_2 are PL decay lifetimes.[69,70] For better comparison between each sample, the average PL decay lifetime was calculated using the following equation:

$$\tau_{avg} = \frac{A_1\tau_1^2 + A_2\tau_2^2}{A_1\tau_1 + A_2\tau_2}$$

The PS-capped $CsPbBr_3$ NCs of different sizes exhibited the average TRPL decay lifetimes of 21.5 ns (D = 8.6 nm), 28.7 ns (D = 10.1 nm), and 44.5 ns (D = 13.9 nm), which agrees well with the reported results in which the increase of NC size leads to the longer lifetimes (i.e., reduced recombination) due to the decreased overlap between the electron and hole wave functions.[70]

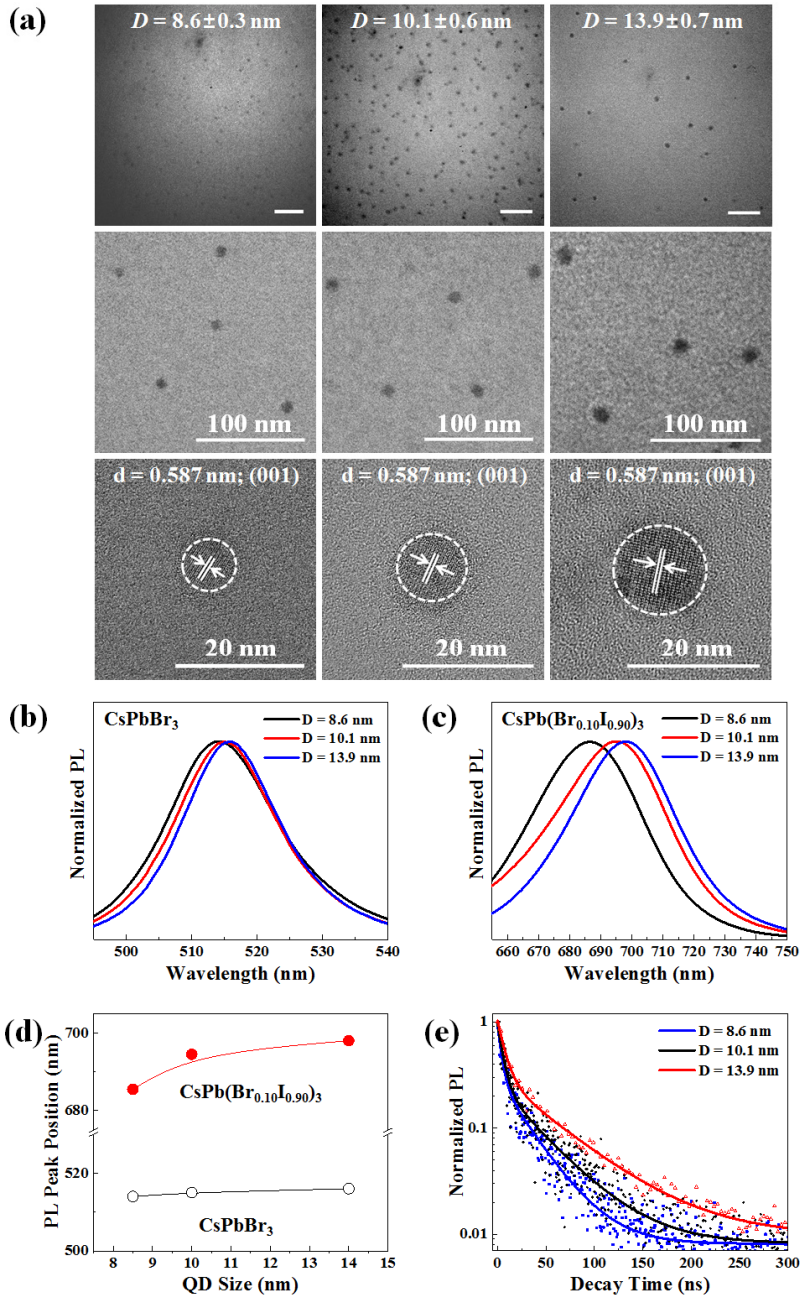

Figure 15. Size-dependent optical properties of PS-capped $CsPbX_3$ NCs. (a) TEM images of PS-capped $CsPbBr_3$ NCs of three different sizes. Column 1: D = 8.6±0.3 nm; crafted using sample 1 in **Table 1**). Column 2: D = 10.1±0.6 nm, crafted using sample 3 in **Table 1**. Column 3: D = 13.9±0.7 nm; crafted using sample 5 in **Table 1.** The corresponding HRTEM images are shown in the last row, where the (001) plane has a lattice spacing d of 0.587 nm. (b) PL spectra of green-emitting PS-capped $CsPbBr_3$ NCs of three different sizes. (c) PL spectra of red-emitting PS-capped $CsPb(Br_{0.1}I_{0.9})_3$ NCs of three different sizes. (d) Effect of NC size on the PL peak position. Open circle: PS-capped $CsPbBr_3$ NCs. Solid circle: PS-capped $CsPb(Br_{0.1}I_{0.9})_3$ NCs. (e) Time-resolved photoluminescence (TRPL) spectroscopy of PS-capped $CsPbBr_3$ NCs of three different sizes.

Figure 16a-16b clearly displays the robustness of the PS shell in protecting the $CsPbBr_3$ NCs from degradation by water. Intriguingly, by increasing the molecular weight (i.e., chain length) of PS blocks, the water stability of PS-capped NCs increased by 33% from 36.3±5.7 min for PS(7k)-capped $CsPbBr_3$ NCs (D = 13.9 nm) to 48.3±0.6 min for PS(16k)-capped $CsPbBr_3$ NC (D = 13.9 nm) (**Figure 16b**; see *Experimental Section*). More interestingly, by decreasing the NC size from 13.9 nm to 8.6 nm while keeping the PS length constant (i.e., $M_{n,\,PS}$ = 16 kg/mol), the water stability increased by 28%, that is, from 48.3±0.6 min for PS(16k)-capped $CsPbBr_3$ NCs (D = 13.9 nm) to 61.7±3.2 min for PS(16k)-capped $CsPbBr_3$ NC (D = 8.6 nm) (**Figure 16b**). Remarkably, in stark contrast to $CsPbBr_3$ NCs synthesized via conventional ligand-assisted co-precipitation methods either capped by oleic acid (2.8±0.3 min) or co-capped by oleic acid and oleyl amine (5.0±0.5 min) (**Figure 16b**), the water stability of PS-capped $CsPbBr_3$ NCs was up to 20 times longer. We note that for the oleic acid- & oleyl amine-co-capped $CsPbBr_3$ NCs, an additional image was taken after removing the stir bar as the NCs formed a thin layer of film on the stir bar which maintained PL for a longer duration than the NCs in toluene.

It is not surprising that PS-capped $CsPbBr_3$ NCs also exhibited superior colloidal stability when stored in toluene (**Figure 16c**). The permanently ligated PS chains on the perovskite NC surface are well dissolved in good solvent, toluene, leading to excellent dispersion of PS-capped $CsPbBr_3$ NCs without aggregation. The QY of PS-capped $CsPbBr_3$ NC in toluene solution was maintained for more than 2 months without any decrease (see *Experimental Section*; **Figure 16c**). It is also notable that there was no significant shift in the PL peak position as well as the FWHM (**Figure 16d-16e**), signifying minimal or no change in the size distribution of NCs over the 2-month period. In sharp contrast, oleic acid-capped $CsPbBr_3$ NCs (see *Experimental Section*; oleic acid-capped $CsPbBr_3$ NCs prepared via a hot-injection method) displayed a PL peak shoulder and a 22% increase in FWHM of PL spectrum only after 24 h storage under ambient conditions (i.e., exposed to air and light at room temperature without stirring). **Figure 16f** shows two representative highly luminescent PS-capped $CsPbBr_3$ NCs in toluene even after 12 months of storage under the same ambient condition as noted above.

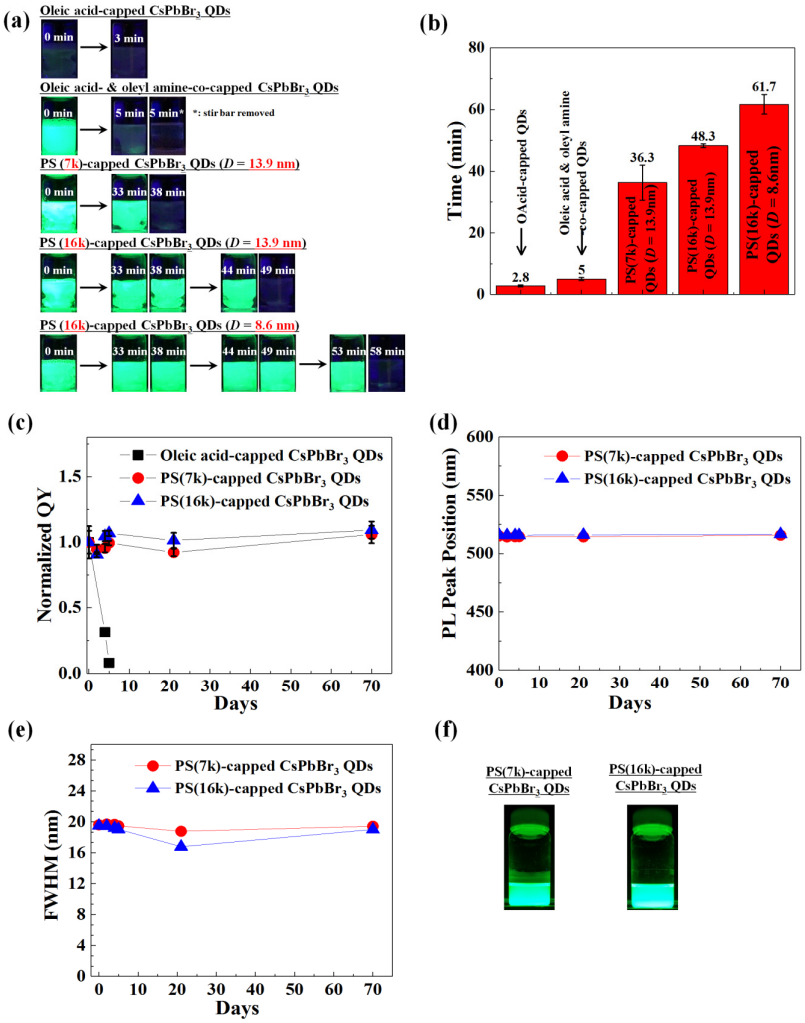

Figure 16. Water and colloidal stability of PS-capped $CsPbBr_3$ NCs. (a-b) Water stability of PS-capped $CsPbBr_3$ NCs. (a) Representative digital images, depicting water stability of $CsPbBr_3$ NCs. The NCs are under UV excitation. The far-right column of each row is the image taken immediately after the sharp and complete disappearance of PL emission. PS(7k)-capped $CsPbBr_3$ NCs (D = 13.9 nm), PS(16k)-capped $CsPbBr_3$ NCs (D = 13.9 nm), and PS(16k)-capped $CsPbBr_3$ NCs (D = 8.6 nm) are crafted using sample 5, sample 6, and sample 2, respectively, in **Table 1** as nanoreactors. (b) Bar graph depicting an average duration of PL emission under constant UV excitation after NCs are exposed to water. The average time was calculated after running each experiment for 5 times. The time for each run is recorded immediately after the complete diminishing of PL emission. (c-f) Colloidal stability of PS-capped PS(7k)-capped and PS(16k)-capped $CsPbBr_3$ NCs crafted using sample 5 and 6, respectively, in **Table 1** as nanoreactors. (c) Quantum yield (QY) of PS-capped $CsPbBr_3$ NCs over 70 days. Oleic acid-capped $CsPbBr_3$ NCs synthesized via hot injection (see *Experimental Section*) was used as control. (d) PL peak position of PS-capped $CsPbBr_3$ NCs over 70 days. (e) FWHM of PS-capped $CsPbBr_3$ NCs over 70 days. (e) PS-capped $CsPbBr_3$ NC toluene solution under UV excitation after 12-month storage under ambient condition (i.e., exposed to air and light at room temperature without stirring).

The markedly improved colloidal and water stabilities of PS-capped NCs can be rationalized as follows. As toluene is a good solvent for PS, the intimately and permanently tethered PS chains on the perovskite NC surface are fully extended as a result of favorable interaction between toluene and PS, yielding excellent colloidal stability. However, when water is introduced, the hydrophobic PS chains collapse onto the perovskite NC due to the poor solubility of PS in water. The collapsed PS chain forms a PS shell surrounding the perovskite NC surface, thereby preventing water from reaching and degrading the perovskite NC due to its ionic nature (**Figure 17b-17d**). It is worth noting that the longer PS chains (16k PS (**Figure 17c)** compared to 7k PS (**Figure 17b)**) impart the denser hydrophobic PS shell situated on the perovskite NC surface and thus further effectively blocks the water penetration through the shell, leading to enhanced stability against water (**Figure 16a-16b**). As the size of NCs capped with the same length of PS chains decreases (13.9-nm compared to 8.6-nm $CsPbBr_3$ NCs capped by 16k PS chains), the surface of NC is further adequately covered by PS, resulting in progressively improved water stability (**Figure 17d** and **Figure 16a-16b**). Clearly, each PS-capped $CsPbBr_3$ NC, for the first time, possesses a separate protective shell that can be precisely tailored to any desired length (or thickness when in contact with water). In contrast to PS-capped $CsPbBr_3$ NCs, due to the weak coordination bonding between small-molecule ligands (e.g., oleic acid & oleyl amine) and NCs, these ligands collapsed on the $CsPbBr_3$ NC surface upon the addition of water would dissociate from the NC surface. Consequently, water contacts the exposed surface of NCs, causing their decomposition into precursors and the diminishing of fluorescence (**Figure 17a**).

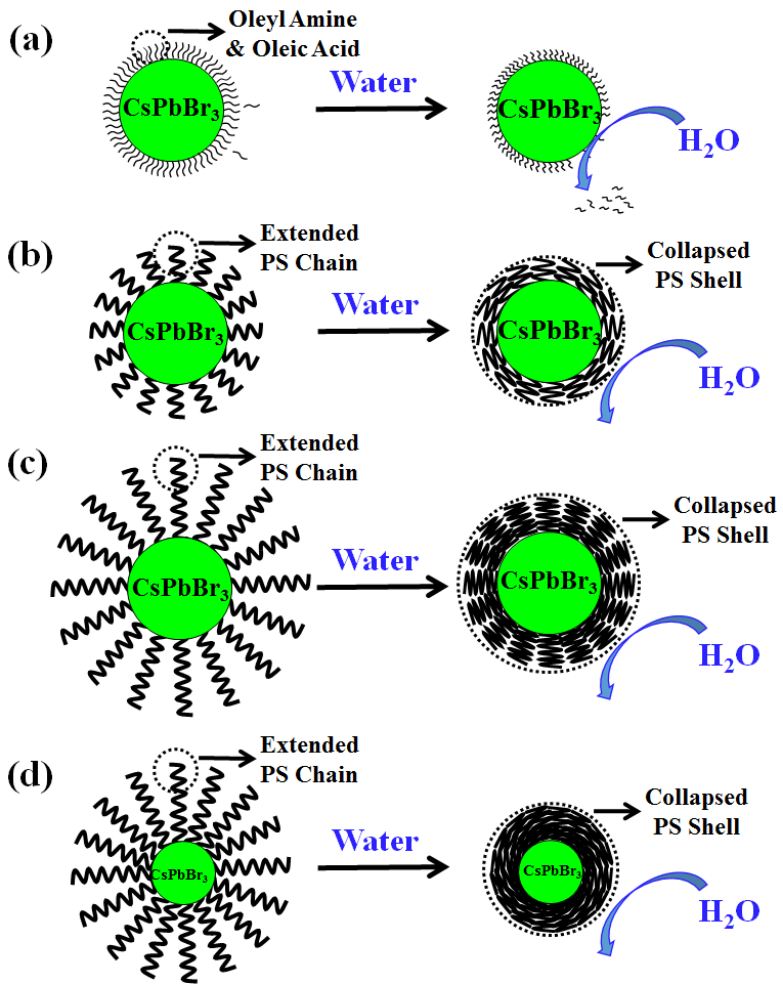

Figure 17. Schematic illustration of PS-capped NCs with varied NC sizes and length of PS chains for markedly improved colloidal and water stabilities. (a) Linear ligand (oleyl amine & oleic acid) loss from the perovskite NC surface upon water exposure in oleyl amine- & oleic acid-co-capped $CsPbBr_3$ NCs. (b-d) Polystyrene chains collapse onto the perovskite NC surface upon water exposure. (b) Permanently-grafted PS(7k) forms a layer of PS shell around $CsPbBr_3$ NC (*D* = 13.9 nm; PS(7k)-capped $CsPbBr_3$ NCs are synthesized using sample 5 in **Table 1**). (c) Permanently-tethered PS(16k) forms a layer of denser PS shell on the surface of $CsPbBr_3$ NC (*D* =13.9 nm; PS(16k)-capped $CsPbBr_3$ NCs are crafted using sample 6 in **Table 1**). (d) Permanently-capped PS(16k) forms a layer of even denser PS shell situated on smaller-sized $CsPbBr_3$ NCs (*D* = 8.6 nm; PS(16k)-capped $CsPbBr_3$ NCs are yielded using sample 2 in **Table 1**)

Due to their high QY, narrow FWHM, size- and composition-dependent emission tunability, and solution processability,[71] perovskite NCs represent next-generation materials for use in display and solid-state lighting. In this context, as as-synthesized PS-capped perovskite NCs show good optical properties, their potential application in white light emitting diode (WLED) was demonstrated (**Figure 18**). A WLED prototype was fabricated by placing a composite of green-emitting PS-capped $CsPbBr_3$ NCs, red-emitting $CdSe/Cd_{1-x}Zn_xSe_{1-y}S_y/ZnS$ NCs synthesized according to a previous work in GT collaborator Dr. Lin's lab,[72] and poly(methyl methacrylate) (PMMA) onto a blue-emitting GaN chip. **Figure 18a** presents the PL spectra of the WLED device

with three distinct peaks from the GaN blue-chip (blue), PS-capped $CsPbBr_3$ NCs (green), and $CdSe/Cd_{1-x}Zn_xSe_{1-y}S_y/ZnS$ NCs (red),[72] respectively. A digital image of an actual WLED device emitting white light is shown as an inset. **Figure 18b** displays the Commission Internationale de L'Eclairage (CIE) diagram. The WLED prototype containing the PS-capped $CsPbBr_3$ NCs has a color coordinate of (0.31, 0.32), which is very close to the white color coordinate of (0.33, 0.33). The color gamut of PS-capped $CsPbBr_3$ NC-based WLED is 116% over that of national television system committee (NTSC) and 163% over that of standard red green blue (sRGB) standards.

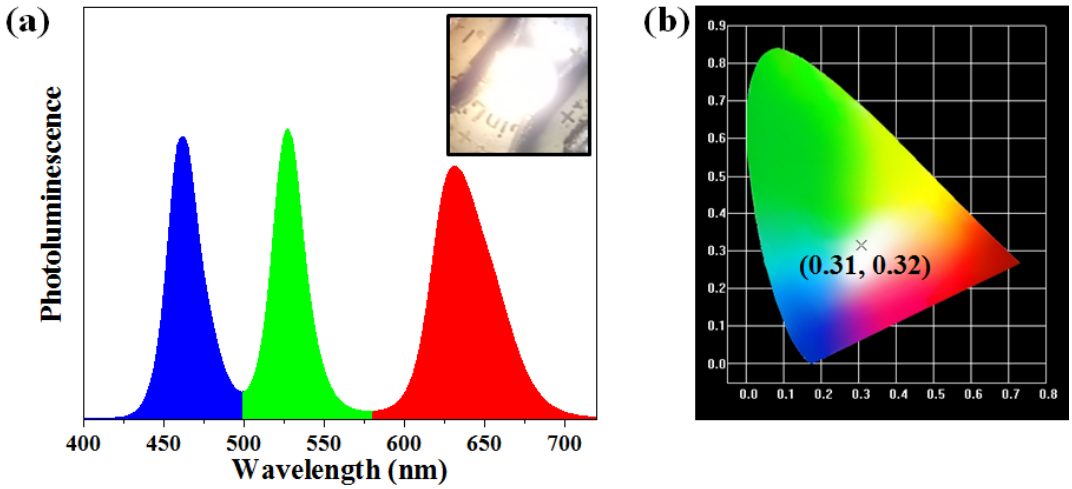

Figure 18. PS-capped $CsPbBr_3$ NC-based white light emitting diode (WLED). (a) PL spectra of PS-capped $CsPbBr_3$ NC-based WLED device operated at a current of 30 mA. Inset shows a digital image of the WLED device. (b) CIE color diagram of the WLED device. The "x" label indicates the color coordinate for the WLED device operated at 30 mA.

Experimental Methods

Synthesis of 21-arm star-like poly(tert-butyl acrylate) (star-like PtBA): Heptakis[2,3,6-tri-O-(2-bromo-2-methylpropionyl)]-β-cyclodextrin (21Br-β-CD) was prepared according to previous reported procedure.[50,51] Star-like P*t*BA was synthesized by atom transfer radical polymerization (ATRP) of tert-butyl acrylate (*t*BA) monomers using 21Br-β-CD macroinitiator. Briefly, CuBr (35.0 mg), PMDETA (85.0 mg), 21Br-β-CD (50 mg), *t*BA (21 mL), and MEK (21 mL) were mixed in an argon bubbled ampoule. The ampoule was then sealed and placed in an oil bath at 60°C. The reaction was later quenched by cooling the ampoule in liquid nitrogen. The solution was then diluted with acetone and passed through an activated neutral alumina column to remove the catalyst, and subsequently underwent fractional precipitation with methanol/water (v/v = 1/1, precipitator) to remove monomers and linear polymers. The product was then dried at 40°C under vacuum for 24 h prior to use.

Synthesis of 21-arm star-like poly(tert-butyl acrylate)-b-polystyrene (star-like PtBA-b-PS): Star-like P*t*BA-*b*-PS was synthesized by ATRP of styrene (St) monomers from star-P*t*BA initiator. Briefly, Star-like P*t*BA-Br (i.e., Br in P*t*BA macroinitiator) : CuBr : PMDETA : St = 1 : 1 : 2 : 800 (molar ratio) in anisole (1ml solvent per 1g St) was placed in an argon bubbled ampoule. The ampoule was then sealed and placed in an oil bath at 90°C. The reaction was later quenched by placing the ampoule in liquid nitrogen. The product solution was diluted with THF and passed through an activated neutral alumina column to remove the catalyst, and subsequently purified by

fractional precipitation with methanol/water (v/v = 1/1) as the precipitator to remove unreacted monomers. The product was then dried at 40°C under vacuum for 24 h prior to use.

Synthesis 21-arm star-like poly(acrylic acid)-b-polystyrene (star-like PAA-b-PS): Star-like PAA-*b*-PS was synthesized by hydrolysis of tert-butyl ester groups of P*t*BA blocks of star-like P*t*BA-*b*-PS to acrylic acid groups. Briefly, star-like P*t*BA-*b*-PS (1 g) was fully dissolved in dichloromethane (200 mL), followed by the addition of trifluoroacetic acid (TFA) (10 mL). The reaction proceeded at room temperature for 24 h. After hydrolysis, the solvent was evaporated under reduced pressure. The final product was washed with dichloromethane and methanol, and thoroughly dried under vacuum at 40 °C for 24 h.

Synthesis of PS-capped $CsPbBr_3$ NCs: Star-PAA-*b*-PS was used as nanoreactor for the synthesis of PS-capped $CsPbBr_3$ NCs. The strong coordination interaction between the metal moieties of $CsPbBr_3$ precursors (i.e., CsBr and $PbBr_2$) and carboxyl groups (-COOH) of the inner hydrophilic PAA blocks of star-like PAA-*b*-PS facilitated the nucleation and growth of $CsPbBr_3$ NCs selectively within the inner compartment occupied by PAA blocks of the nanoreactor. In a typical procedure, star-like PAA-*b*-PS was dissolved in DMF at room temperature, followed by the addition of CsBr and $PbBr_2$. To allow ample time for the precursors to diffuse into the inner PAA compartment of the nanoreactor, the solution was stirred for 12 h. The precursor solution was then dropped into toluene, upon which PS-capped $CsPbBr_3$ NCs immediately formed in solution. Although toluene is a poor solvent for perovskite NCs, the PS-capped $CsPbBr_3$ NCs were colloidally stable due to the permanently tethered PS chain situated on the NC surface.

Phase I Work Summary:

Stability enhancement of perovskite NCs via encapsulation in metal stearate

In summary, we have developed a simple yet robust strategy to craft a new class of $CsPbX_3$–MSt nanocomposite powder phosphors (where X = Br, I, or Br/I; M = Na, Zn and Al) with a set of impressive stabilities. These are: high water stability, compositional stability, phase stability, and phase segregation stability for SSL applications. Notably, this strategy allows for rapid and effective precipitation and purification of $CsPbX_3$ NCs from the crude solution, thus eliminating the need for polar solvents widely used for yielding perovskite NCs and in turn preventing the damage of $CsPbX_3$ NCs. Due to insolubility of $AlSt_3$ in water, the resulting $CsPbX_3$–$AlSt_3$ nanocomposites retain their high emission in water, that is, a demonstration of water stability. Moreover, when mixing $CsPbBr_3$–$AlSt_3$ and $CsPbI_3$–$AlSt_3$ nanocomposites together, anion exchange between them (i.e., Br^- and I^- exchange) is virtually arrested because of the efficient coating and separation of the respective $CsPbX_3$ by $AlSt_3$, that is, a manifestation of compositional stability. Furthermore, for $CsPbI_3$ NCs, cubic phase is metastable at room temperature and readily transformed into PL-inactive orthorhombic phase. After coating with $AlSt_3$, the resulting $CsPbI_3$–$AlSt_3$ nanocomposites preserve the cubic phase of $CsPbI_3$ and high emission for at least one month, that is, a representation of phase stability. Finally, $CsPbBr_{1.5}I_{1.5}$ NCs impregnated within $AlSt_3$ matrix sustain high emission without degradation for at least one month, that is, a display of phase segregation stability. These optically-active, highly stable nanocomposites are exploited as solid-state luminophores for white LED and RadiantFlex sheets, delivering the appreciable performance, including a high Ra of 89.9, a low Tc of 4588 K and LER up to 332 lm/W. By extension, this simple strategy may be properly applied to other functional yet

less stable NC systems, for example, organic-inorganic perovskite NCs and inorganic nonlead-based perovskite NCs for a wide range of applications in optoelectronic materials and devices.

Stability enhancement of perovskite NCs at single particle level via permanently ligating with polymer hair

In summary, we have demonstrated the precision synthesis of perovskite NCs of varies sizes and compositions permanently anchored by hydrophobic polymer chains via capitalizing on judiciously designed amphiphilic star-like diblock copolymers as nanoreactors. The polymer nanoreactors are synthesized via sequential ATRP of *t*BA and St from a macroinitiator with multiple activation sites, yielding star-like P*t*BA-*b*-PS, followed by hydrolysis of the inner P*t*BA blocks. Due to living free radical polymerization characteristic, ATRP entails the synthesis of star-like diblock copolymer with well-controlled molecular weight and low PDI of each block. Consequently, the size of PS-capped perovskite $CsPbX_3$ NCs, formed via strong coordination interaction of perovskite precursors with the inner hydrophilic PAA blocks of star-like PAA-*b*-PS, can be precisely tailored, thereby offering delicate control over absorption and emission of $CsPbX_3$ NCs. Green-emitting crafted PS-capped $CsPbBr_3$ NCs exhibit a high PL QY of 69% and low FWHM of 17.7 nm. Notably, subsequent anion exchange of the halide group renders a process of effectively tuning the emission of PS-capped NCs from 427 nm (blue) to 700 nm (red). It is important to note that this process results in each PS-capped $CsPbX_3$ NC, carrying a layer of protective hydrophobic PS chains that can be readily regulated to any desired length during the ATRP of St monomers. Such permanently ligated length-tunable PS shells on the $CsPbX_3$ surface affords strikingly improved water and colloidal stabilities in harsh environment (e.g., deliberately added water) that is often not experienced under regular operating conditions. When directly exposed to water, the PS chains collapse onto the perovskite NC due to its poor solubility in water, forming a dense PS cushion on the perovskite NC surface and thus greatly preventing water from reaching and dissolving the perovskite NC. In striking contrast to $CsPbBr_3$ NCs synthesized via conventional ligand-assisted approaches, PS-capped $CsPbBr_3$ NCs impart a twentyfold improvement in water stability. In addition, PS-capped $CsPbBr_3$ NCs also manifest superior colloidal stability when stocked in toluene and exposed to air under constant ambient light at room temperature without stirring. This can be attributed to the fact that the perovskite NCs are intimately and stably ligated by PS chains that are fully extended in good solvent toluene. As a result, PS-capped $CsPbBr_3$ NCs demonstrated excellent colloidal stability for more than 2 months with no change in QY, PL peak position and FWHM. WLEDs constructed using hairy perovskite NCs demonstrated a 116% and 163% color gamut over NTSC and sRGB standards, respectively.

Planned Future Work:

In the proposed future study, the metal stearate encapsulation method will be further optimized for the large scale fabrication of perovskite NC-MSt nanocomposite powder phosphors. The PS-tethered perovskite NCs may facilitate uniform dispersion in polymer matrix, thus reducing or virtually eliminating enthalpic interactions of hairy perovskite NCs with the host matrix for uniform perovskite NCs/polymer nanocomposites. To further improve performance for lighting applications, the outer PS blocks of star-like diblock copolymer nanoreactor can be replaced by polymers with superior optical stability such as polydimethylsiloxane (PDMS) to improve optical and thermal stability. In addition, a hermetical duel-shell perovskite/SiO_2/PDMS NC structure will

be fabricated to further improve stability. Finally, new down-converting RadiantFlex sheets with maximum luminous efficacy over a broad temperature and optical flux range will be fabricated utilizing the new classes of perovskites NC phosphors developed in this program. This approach facilitates us to capitalize both on the advantages of PTC's *RadiantFlex* sheet technology (including *color uniformity with angles, low scattering loss, high efficacy and flexibility*) and that of this new class of perovskite materials. While the perovskite materials could be used *to minimize scattering losses and enhance LER*, our controlled sheet manufacturing methods will allow us to design, formulate, optimize and manufacture the newly proposed customizable RadiantFlex sheets (with desirable CCT and CRI values) at affordable cost.

References

(1) Kagan, C.; Mitzi, D.; Dimitrakopoulos, C. *Science* **1999**, *286*, 945.

(2) Lee, M.; Teuscher, J.; Miyasaka, T.; Murakami, T.; Snaith, H. *Science* **2012**, *338*, 643.

(3) Jeon, N.; Noh, J.; Kim, Y.; Yang, W.; Ryu, S.; Seok, S. *Nat. Mater.* **2014**, *13*, 897.

(4) Green, M.; Ho-Baillie, A.; Snaith, H. *Nat. Photon.* **2014**, *8*, 506.

(5) Kim, H.; Ohkita, H.; Benten, H.; Ito, S. *Adv. Mater.* **2016**, *28*, 917.

(6) Raja, S. N.; Bekenstein, Y.; Koc, M. A.; Fischer, S.; Zhang, D.; Lin, L.; Ritchie, R. O.; Yang, P.; Alivisatos, A. P. *ACS Appl. Mater. Interfaces* **2016**, *8*, 35523.

(7) Chen, J.; Shi, T.; Li, X.; Zhou, B.; Cao, H.; Wang, Y. *Appl. Phys. Lett.* **2016**, *108*, 053302.

(8) McMeekin, D.; Sadoughi, G.; Rehman, W.; Eperon, G.; Saliba, M.; Horantner, M.; Haghighirad, A.; Sakai, N.; Korte, L.; Rech, B.; Johnston, M.; Herz, L.; Snaith, H. *Science* **2016**, *351*, 151.

(9) Zhou, H.; Chen, Q.; Li, G.; Luo, S.; Song, T.; Duan, H.; Hong, Z.; You, J.; Liu, Y.; Yang, Y. *Science* **2014**, *345*, 542.

(10) Yang, W.; Noh, J.; Jeon, N.; Kim, Y.; Ryu, S.; Seo, J.; Seok, S. *Science* **2015**, *348*, 1234.

(11) Nedelcu, G.; Protesescu, L.; Yakunin, S.; Bodnarchuk, M.; Grotevent, M.; Kovalenko, M. *Nano Lett.* **2015**, *15*, 5635.

(12) Zhang, X.; Lin, H.; Huang, H.; Reckmeier, C.; Zhang, Y.; Choy, W.; Rogach, A. *Nano Lett.* **2016**, *16*, 1415.

(13) Tian, Y.; Merdasa, A.; Peter, M.; Abdellah, M.; Zheng, K.; Ponseca, C.; Pullerits, T.; Yartsev, A.; Sundstrom, V.; Scheblykin, I. *Nano Lett.* **2015**, *15*, 1603.

(14) Cha, M.; Da, P.; Wang, J.; Wang, W.; Chen, Z.; Xiu, F.; Zheng, G.; Wang, Z. *J. Am. Chem. Soc.* **2016**, *138*, 8581.

(15) Eaton, S.; Lai, M.; Gibson, N.; Wong, A.; Dou, L.; Ma, J.; Wang, L.; Leone, S.; Yang, P. *PNAS* **2016**, *113*, 1993.

(16) Fu, Y.; Zhu, H.; Schrader, A.; Liang, D.; Ding, Q.; Joshi, P.; Hwang, L.; Zhu, X.; Jin, S. *Nano Lett.* **2016**, *16*, 1000.

(17) Zhu, H.; Fu, Y.; Meng, F.; Wu, X.; Gong, Z.; Ding, Q.; Gustafsson, M.; Trinh, M.; Jin, S.; Zhu, X. *Nat. Mater.* **2015**, *14*, 636.

(18) Wang, Y.; Zhu, Y.; Huang, J.; Cai, J.; Zhu, J.; Yang, X.; Shen, J.; Jiang, H.; Li, C. *J. Phys. Chem. Lett.* **2016**, *7*, 4253.

(19) Li, Q.-L.; Lu, W.-X.; Wan, N.; Ding, S.-N. *Chem. Commun.* **2016**, *52*, 12342.

(20) Akkerman, Q. A.; D'Innocenzo, V.; Accornero, S.; Scarpellini, A.; Petrozza, A.; Prato, M.; Manna, L. *J. Am. Chem. Soc.* **2015**, *137*, 10276.

(21) Roo, J.; Ibanez, M.; Geiregat, P.; Nedelcu, G.; Walravens, W.; Maes, J.; Martins, J.; Driessche, I.; Kovalenko, M.; Hens, Z. *ACS Nano* **2016**, *10*, 2071.

(22) Wang, C.; Chesman, A. S.; Jasieniak, J. J. *Chemical Communications* **2017**, *53*, 232.

(23) Wei, S.; Yang, Y.; Kang, X.; Wang, L.; Huang, L.; Pan, D. *Chemical Communications* **2016**, *52*, 7265.

(24) Wei, Y.; Deng, X.; Xie, Z.; Cai, X.; Liang, S.; Ma, P. a.; Hou, Z.; Cheng, Z.; Lin, J. *Adv. Funct. Mater.* **2017**, *27*, 1703535.

(25) Akkerman, Q. A.; Rainò, G.; Kovalenko, M. V.; Manna, L. *Nature Materials* **2018**, 1.

(26) De Roo, J.; Ibáñez, M.; Geiregat, P.; Nedelcu, G.; Walravens, W.; Maes, J.; Martins, J. C.; Van Driessche, I.; Kovalenko, M. V.; Hens, Z. *ACS nano* **2016**, *10*, 2071.

(27) Kim, Y.; Yassitepe, E.; Voznyy, O.; Comin, R.; Walters, G.; Gong, X.; Kanjanaboos, P.; Nogueira, A. F.; Sargent, E. H. *ACS applied materials & interfaces* **2015**, *7*, 25007.

(28) Nedelcu, G.; Protesescu, L.; Yakunin, S.; Bodnarchuk, M. I.; Grotevent, M. J.; Kovalenko, M. V. *Nano Letters* **2015**, *15*, 5635.

(29) Zhang, T.; Li, G.; Chang, Y.; Wang, X.; Zhang, B.; Mou, H.; Jiang, Y. *CrystEngComm* **2017**, *19*, 1165.

(30) Akkerman, Q. A.; D'Innocenzo, V.; Accornero, S.; Scarpellini, A.; Petrozza, A.; Prato, M.; Manna, L. *Journal of the American Chemical Society* **2015**, *137*, 10276.

(31) Gomez, L.; de Weerd, C.; Hueso, J. L.; Gregorkiewicz, T. *Nanoscale* **2017**, *9*, 631.

(32) Protesescu, L.; Yakunin, S.; Bodnarchuk, M. I.; Krieg, F.; Caputo, R.; Hendon, C. H.; Yang, R. X.; Walsh, A.; Kovalenko, M. V. *Nano letters* **2015**, *15*, 3692.

(33) Luo, P.; Xia, W.; Zhou, S.; Sun, L.; Cheng, J.; Xu, C.; Lu, Y. *The journal of physical chemistry letters* **2016**, *7*, 3603.

(34) Eperon, G. E.; Paterno, G. M.; Sutton, R. J.; Zampetti, A.; Haghighirad, A. A.; Cacialli, F.; Snaith, H. J. *Journal of Materials Chemistry A* **2015**, *3*, 19688.

(35) Seth, S.; Mondal, N.; Patra, S.; Samanta, A. *The journal of physical chemistry letters* **2016**, *7*, 266.

(36) Huang, H.; Chen, B.; Wang, Z.; Hung, T. F.; Susha, A. S.; Zhong, H.; Rogach, A. L. *Chemical Science* **2016**, *7*, 5699.

(37) Wang, H. C.; Lin, S. Y.; Tang, A. C.; Singh, B. P.; Tong, H. C.; Chen, C. Y.; Lee, Y. C.; Tsai, T. L.; Liu, R. S. *Angewandte Chemie International Edition* **2016**, *55*, 7924.

(38) Swarnkar, A.; Marshall, A. R.; Sanehira, E. M.; Chernomordik, B. D.; Moore, D. T.; Christians, J. A.; Chakrabarti, T.; Luther, J. M. *Science* **2016**, *354*, 92.

(39) Loiudice, A.; Saris, S.; Oveisi, E.; Alexander, D. T. L.; Buonsanti, R. *Angew. Chem. Int. Ed.* **2017**, *56*, 10696.

(40) Hu, H.; Wu, L.; Tan, Y.; Zhong, Q.; Chen, M.; Qiu, Y.; Yang, D.; Sun, B.; Zhang, Q.; Yin, Y. *J. Am. Chem. Soc.* **2018**, *140*, 406.

(41) Xin, Y.; Zhao, H.; Zhang, J. *ACS Appl. Mater. Interfaces* **2018**, *10*, 4971.

(42) Zhang, H.; Wang, X.; Liao, Q.; Xu, Z.; Li, H.; Zheng, L.; Fu, H. *Adv. Funct. Mater.* **2017**, *27*, 1604382.

(43) Wang, H.-C.; Lin, S.-Y.; Tang, A.-C.; Singh, B. P.; Tong, H.-C.; Chen, C.-Y.; Lee, Y.-C.; Tsai, T.-L.; Liu, R.-S. *Angew. Chem. Int. Ed.* **2016**, *55*, 7924.

(44) Van der Stam, W.; Geuchies, J. J.; Altantzis, T.; Van Den Bos, K. H.; Meeldijk, J. D.; Van Aert, S.; Bals, S.; Vanmaekelbergh, D.; de Mello Donega, C. *Journal of the American Chemical Society* **2017**, *139*, 4087.

(45) Goldschmidt, V. M. *Naturwissenschaften* **1926**, *14*, 477.

(46) Green, M. A.; Ho-Baillie, A.; Snaith, H. J. *Nature Photonics* **2014**, *8*, nphoton. 2014.134.

(47) Brandt, R. E.; Stevanović, V.; Ginley, D. S.; Buonassisi, T. *Mrs Communications* **2015**, *5*, 265.

(48) Yang, Y.; Qin, H.; Jiang, M.; Lin, L.; Fu, T.; Dai, X.; Zhang, Z.; Niu, Y.; Cao, H.; Jin, Y. *Nano letters* **2016**, *16*, 2133.

(49) Chen, W.; Hao, J.; Hu, W.; Zang, Z.; Tang, X.; Fang, L.; Niu, T.; Zhou, M. *Small* **2017**, *13*.

(50) Pang, X.; Zhao, L.; Akinc, M.; Kim, J. K.; Lin, Z. *Macromolecules* **2011**, *44*, 3746.

(51) Pang, X.; Zhao, L.; Feng, C.; Lin, Z. *Macromolecules* **2011**, *44*, 7176.

(52) Pang, X.; Zhao, L.; Han, W.; Xin, X.; Lin, Z. *Nat. Nanotech.* **2013**, *8*, 426.

(53) Zheng, D.; Pang, X.; Wang, M.; He, Y.; Lin, C.; Lin, Z. *Chem. Mater.* **2015**, *27*, 5271.

(54) Xu, H.; Xu, Y.; Pang, X.; He, Y.; Jung, J.; Xia, H.; Lin, Z. *Sci. Adv.* **2015**, *1*, e1500025.

(55) Xu, H.; Pang, X.; He, Y.; He, M.; Jung, J.; Xia, H.; Lin, Z. *Angew. Chem. Int. Ed.* **2015**, *54*, 4636.

(56) Yang, D.; Pang, X.; He, Y.; Wang, Y.; Chen, G.; Wang, W.; Lin, Z. *Angew. Chem. Int. Ed.* **2015**, *54*, 12091.

(57) Pang, X.; He, Y.; Jung, J.; Lin, Z. *Science* **2016**, *353*, 1268.

(58) Wang, M.; Pang, X.; Zheng, D.; He, Y.; Sun, L.; Lin, C.; Lin, Z. *J. Mater. Chem. A* **2016**, *4*, 7190.

(59) Jiang, B.; Pang, X.; Li, B.; Lin, Z. *J. Am. Chem. Soc.* **2015**, *137*, 11760.

(60) Hou, S.; Guo, Y.; Tang, Y.; Quan, Q. *ACS Appl. Mater. Interfaces* **2017**, *9*, 18417.

(61) Chen, Y.; Yang, D.; Yoon, Y. J.; Pang, X.; Wang, Z.; Jung, J.; He, Y.; Harn, Y. W.; He, M.; Zhang, S.; Zhang, G.; Lin, Z. *J. Am. Chem. Soc.* **2017**, *139*, 12956.

(62) Chen, Y.; Wang, Z.; He, Y.; Yoon, Y. J.; Jung, J.; Zhang, G.; Lin, Z. *PNAS* **2018**, *115*, E1391.

(63) Li, X.; Wu, Y.; Zhang, S.; Cai, B.; Gu, Y.; Song, J.; Zeng, H. *Adv. Funct. Mater.* **2016**, *26*, 2435.

(64) Yassitepe, E.; Yang, Z.; Voznyy, O.; Kim, Y.; Walters, G.; Castañeda, J. A.; Kanjanaboos, P.; Yuan, M.; Gong, X.; Fan, F.; Pan, J.; Hoogland, S.; Comin, R.; Bakr, O. M.; Padilha, L. A.; Nogueira, A. F.; Sargent, E. H. *Adv. Funct. Mater.* **2016**, *26*, 8757.

(65) Krieg, F.; Ochsenbein, S. T.; Yakunin, S.; ten Brinck, S.; Aellen, P.; Süess, A.; Clerc, B.; Guggisberg, D.; Nazarenko, O.; Shynkarenko, Y.; Kumar, S.; Shih, C.-J.; Infante, I.; Kovalenko, M. V. *ACS Energy Lett.* **2018**, *3*, 641.

(66) Pan, J.; Sarmah, S. P.; Murali, B.; Dursun, I.; Peng, W.; Parida, M. R.; Liu, J.; Sinatra, L.; Alyami, N.; Zhao, C.; Alarousu, E.; Ng, T. K.; Ooi, B. S.; Bakr, O. M.; Mohammed, O. F. *J. Phys. Chem. Lett.* **2015**, *6*, 5027.

(67) Kang, J.; Wang, L.-W. *J. Phys. Chem. Lett.* **2017**, *8*, 489.

(68) Swarnkar, A.; Ravi, V. K.; Nag, A. *ACS Energy Lett.* **2017**, *2*, 1089.

(69) Liu, C.; Li, Z.; Hajagos, T. J.; Kishpaugh, D.; Chen, D. Y.; Pei, Q. *ACS Nano* **2017**, *11*, 6422.

(70) Shinde, A.; Gahlaut, R.; Mahamuni, S. *J. Phys. Chem. C* **2017**, *121*, 14872.

(71) Chiba, T.; Hoshi, K.; Pu, Y.-J.; Takeda, Y.; Hayashi, Y.; Ohisa, S.; Kawata, S.; Kido, J. *ACS Appl. Mater. Interfaces* **2017**, *9*, 18054.

(72) Jung, J.; Lin, C. H.; Yoon, Y. J.; Malak, S. T.; Zhai, Y.; Thomas, E. L.; Vardeny, V.; Tsukruk, V. V.; Lin, Z. *Angew. Chem. Int. Ed.* **2016**, *55*, 5071.